Structural and magnetic isomers of small Pd and Rh clusters: an *ab initio* density functional study

2005 J. Phys.: Condens. Matter 17 5927

(http://iopscience.iop.org/0953-8984/17/38/001)

INSTITUTE OF PHYSICS PUBLISHING JOURNAL OF PHYSICS: CONDENSED MATTER

J. Phys.: Condens. Matter **17** (2005) 5927–5963 doi:10.1088/0953-8984/17/38/001

Structural and magnetic isomers of small Pd and Rh clusters: an *ab initio* density functional study

T Futschek, M Marsman and J Hafner

Institut für Materialphysik and Centre for Computational Materials Science, Universität Wien, Sensengasse 8/12, A-1090 Wien, Austria

Received 10 June 2005, in final form 19 July 2005
Published 9 September 2005
Online at stacks.iop.org/JPhysCM/17/5927

Abstract

We present a comprehensive investigation of the structural, electronic, and magnetic properties of Pd_N and Rh_N clusters with up to $N = 13$ atoms, based on *ab initio* density functional calculations. The novel aspects of our investigation are the following. (i) The structural optimization of the cluster by a symmetry-unconstrained static total-energy minimization has been supplemented for larger clusters ($N \geqslant 7$) with a search for the ground state structure by dynamical simulated annealing. The dynamical structural optimization has led to the discovery of highly unexpected ground state configurations. (ii) The spin-polarized calculations were performed in a fixed-moment mode. This allowed us to study coexisting magnetic isomers and led to a deeper insight into the importance of magnetostructural effects. For both Pd and Rh the larger clusters adopt ground state structures that can be considered as fragments of the face-centred cubic crystal structure of the bulk phase. For Pd clusters, the magnetic ground state is a spin triplet ($S = 1$) for $N \leqslant 9$, a spin quintuplet ($S = 2$) for $N = 10$, and a spin septet ($S = 3$) for the largest clusters. Large magnetic moments with up to $S = 8$ have been found for Rh clusters. Magnetic energy differences have been found to be small, such that there is an appreciable probability of finding excited magnetic isomers even at ambient temperatures. In several cases, the structural energy differences are also sufficiently small to permit the coexistence of polytypes.

(Some figures in this article are in colour only in the electronic version)

1. Introduction

The investigation of the physico-chemical properties of small metallic clusters is a very active field of research, for many reasons. For example, metallic clusters are known to possess unique catalytic properties. Ultrafine dispersed Pd clusters supported on alumina were found to be better CO oxidation catalysts [1] than single crystals of Pd, and also show an enhanced activity for the reduction of nitric oxide by carbon monoxide [2], as well as a higher activity and better selectivity in hydrogenation processes [3]. Another reason for the current interest

in metallic clusters is their fascinating magnetic properties. It is now well known that, in addition to the common ferromagnetic metals Fe, Co, and Ni, some transition metals that are non-magnetic in the bulk may become magnetic when the dimensionality is reduced, as in ultrathin films [4–6], in nanowires [7–9], and in clusters [10–13]. An important factor distinguishing clusters from other low-dimensional structures is the possibility of assuming non-crystallographic (icosahedral, dodecagonal, or other) arrangements, while for ultrathin films and nanowires, the structure of the adsorbate is determined by the epitaxial relation with the support. Non-crystallographic symmetry, together with variations in bond lengths and coordination, could lead to important changes in the electronic properties, with significant consequences for the magnetic and chemical properties.

Experimentally, 4d metals from the end of the transition series have been investigated most extensively. While for Rh clusters large magnetic moments have been reported [10, 11], the magnetism of small Pd clusters remains a controversial issue. Early Stern–Gerlach experiments showed the absence of magnetic moments in Pd clusters [10, 11, 14]. Photoemission experiments [12] suggested a Ni-like spin distribution in Pd_n clusters with $n \leqslant 6$, and non-magnetic behaviour for $n \geqslant 15$. In contrast, dc susceptibility measurements [15] found magnetic moments of $0.23 \pm 0.19\ \mu_B$/atom in Pd clusters with diameters in the range of 50–70 Å. A large number of theoretical studies [16–28] have been devoted to the investigation of Pd clusters. These studies are based on a wide variety of different approaches, ranging from multi-configuration self-consistent field calculations for the smallest clusters [16–18] over density functional calculations for small and medium sized aggregates [19–25] to extended Hückel [26] and tight binding methods [27, 28] applied to large clusters. Rh clusters have also been studied using various techniques [13, 29–38]. The central problem of theoretical cluster studies is the determination of the ground state geometry—with increasing cluster size the number of conceivable configurations increases tremendously. Experimental information is only indirect and in most cases not sufficient for determining the structure precisely. *Ab initio* density functional calculations mostly follow a strategy of optimizing the structure of different isomers under the constraint of conserving point group symmetry. While this is an acceptable procedure for those numbers of atoms allowing for the formation of compact, close-packed structures that can be expected to be favoured by a substantial structural energy difference, it is not very likely that the ground state will be found in clusters where one or two atoms have been added to or subtracted from a compact cluster. In addition, there are indications of the coexistence of structural isomers. For this reason attempts have been made to combine *ab initio* electronic structure calculations with force field molecular dynamics simulations for the cluster structure. However, this strategy is limited by the fact that force fields do not account for the correlation between structure and interatomic forces. Furthermore in clusters not only structural, but also magnetic isomers can exist. It has been demonstrated [23, 35] that different magnetizations can lead to different bond lengths and different geometries. The present work is devoted to extensive investigations of structural and magnetic isomers in Pd and Rh clusters with up to 13 atoms.

Our investigations are based on *ab initio* molecular dynamics using spin density functional theory with gradient-corrected exchange–correlation functionals, supplementing the static optimization of the cluster structure with dynamical simulated annealing calculations to verify the dynamical stability of the optimized structures. The calculations are performed in a fixed-moment mode. This allows us to perform an independent structural optimization of spin isomers and to explore the correlation between magnetism and geometric structure. An important result of our study is that, especially for the larger clusters, not only do energetically almost degenerate magnetic isomers exist, but also the structural energy differences between certain isomers are small enough to allow two or more structural isomers to occur at ambient

temperatures. This coexistence of structural and magnetic isomers must be taken into account when theoretical predictions are confronted with experimental observations. Our paper is organized as follows. In section 2 we review very briefly our methodology for *ab initio* density functional calculations. In section 3 we present an overview of the stable cluster structures, binding energies, magnetic moments, and HOMO–LUMO gaps as a function of cluster size. In section 4 we discuss the results for individual clusters, in particular their atomic and magnetic structures and the correlation between structure and magnetism. Because of the large amount of information contained in our data, only the most important results can be reproduced in this paper—additional material can be found on our Web-site [39]. An analysis of the possible coexistence of magnetic and structural isomers at finite temperatures, together with concluding remarks, is presented in section 5.

2. Computational method

All calculations were performed using the Vienna *Ab initio* Simulation Package (VASP) [40–43]. VASP is based on density functional theory (DFT) theory and works in a plane wave basis set. The electronic ground state is determined by solving the Kohn–Sham equations using an iterative unconstrained band-by-band matrix diagonalization scheme based on a residual minimization method [42, 44]. Exchange and correlation were treated in the generalized gradient approximation (GGA), based on the parametrization by Perdew and Zunger [45] of the local density functional of Ceperley and Alder [46], with the gradient corrections following Perdew and Wang [47]. Spin polarization was taken into account according to Von Barth and Hedin's [48] local spin density theory, using the spin interpolation proposed by Vosko *et al* [49]. The electron–ion interaction was described by the full-potential all-electron projector augmented wave (PAW) method, introduced by Blöchl [50], as implemented in VASP by Kresse and Joubert [51].

The use of DFT calculations requires some comments. The first concerns Jahn–Teller distortions [52] of the cluster structure which are expected to occur if the HOMO is degenerate and only partially occupied. It is important to emphasize that conventional DFT calculations do not produce Jahn–Teller distortions, because the electron density is described by single-determinant states [53]. The correct description of these effects requires higher-level quantum chemical descriptions representing electron densities in terms of weighted averages of the degenerate single-determinant states. The second remark concerns the notorious tendency of DFT to underestimate the width of the HOMO–LUMO gap. Improved values for the gap may be achieved using GW calculations [54], by introducing self-interaction corrections (SIC) [55], or by using hybrid functionals mixing exact (Hartree–Fock) and DFT exchange like in the B3LYP functional [56, 57]. GW and SIC calculations are usually applied as *a posteriori* corrections to DFT-optimized geometries. Due to the admixture of exact exchange, the computational effort required for calculations using hybrid functionals is dramatically increased compared to that for standard DFT. At an even higher level of theory, Hartree–Fock configuration interaction (HF-CI) or multi-configuration self-consistent field (MSCSCF) calculations [17, 18] may be performed—albeit at the cost of an even larger computational effort. Calculations using hybrid functionals have been performed for selected geometries of very small clusters [20], MCSCF studies have been extended only up to four-atom clusters [17]. As the main thrust of this paper is the investigation of the structure–property relationship as a function of cluster size, all calculations have been performed with gradient-corrected DFT functionals. The possible importance of Jahn–Teller distortions is discussed where appropriate.

To explore coexisting magnetic isomers, all spin-polarized calculations have been performed in a fixed-moment mode. The total magnetic moment M of a cluster may be

constrained to a fixed value by adding the constraint via a Lagrange multiplier λ, the total energy being given by [58]

$$E(M) = \min\left\{E[n(\vec{r}), m(\vec{r})] + \lambda\left[\int_V m(\vec{r})\,\mathrm{d}^3r - M\right]\right\}.$$

Here $n(\vec{r})$ and $m(\vec{r})$ represent the charge and spin densities of the system and physically the Lagrange multiplier λ represents a magnetic field acting on the electrons. Alternatively, the difference in number of electrons occupying the spin-up and spin-down eigenstates (and hence the magnetic moment M) may be constrained to a fixed value [59, 60]. This is equivalent to introducing two Fermi energies $E_\mathrm{F}^\pm$ for both spin directions and is equivalent to the Lagrange multiplier method if the volume V of integration extends over the entire system; in this case $E_\mathrm{F}^\pm = E_\mathrm{F} \pm \lambda$. Here we follow the computationally less demanding approach of Williams *et al* [59] to fix the occupation number in the two spin channels. Local magnetic moments have been calculated by projecting the plane wave components of the spin-polarized eigenstates on spherical waves within atomic spheres and integrating the resulting local spin-polarized densities of states up to the Fermi level. The atomic sphere radius has been chosen such that the local moments sum to the correct value for the total moment. However, it must be emphasized that for complex magnetization densities with a substantial antiferromagnetic component this is not always possible. In these cases the local magnetic moments must be considered as semiquantitative estimates, but this occurs only in a very few exceptional cases.

For a number of low-spin isomers the calculations show the coexistence of spin-up and spin-down components in the magnetization densities, and hence of a certain competition between ferromagnetic and antiferromagnetic exchange interactions which could, in principle, lead to the formation of a non-collinear magnetic structure. For very small Fe_N and Cr_N clusters with up to $N = 5$ atoms, Hobbs *et al* [61] have investigated collinear and non-collinear magnetic structures using the unconstrained vector field description of magnetism implemented in VASP. A non-collinear ground state was found only for Fe_5 with the structure of a trigonal bipyramid. In all other cases, a structurally distorted cluster with a collinear magnetic structure was found to be lower in energy than the more symmetric cluster where the magnetic frustration is released by a canting of the magnetic moments. For this reason, and because the simultaneous optimization of the geometric structure and non-collinear magnetic moments leads to a strongly increased computational workload, all calculations have been performed for collinear magnetic moments.

The plane wave basis set included plane waves up to a kinetic energy cut-off of 250 eV. For clusters consisting of two to ten atoms a $10 \times 10 \times 10$ Å^3 cubic supercell was used (this was found to be large enough to ensure that the periodically repeated cluster images do not interact with each other). For clusters consisting of more than ten atoms per supercell a $15 \times 15 \times 15$ Å^3 cubic supercell was used. Electronic eigenstates have been calculated at the centre of the Brillouin zone of the supercell only. To improve convergence, a modest Gaussian smearing ($\sigma = 0.02$ eV) has been used for the calculation of the electronic density of states.

The geometry of the clusters has been determined by static relaxation, using a conjugate-gradient minimization and the exact Hellmann–Feynman forces. For the smallest clusters (up to six atoms) it was found to be sufficient to optimize the geometries of a few structural isomers, allowing several spin isomers for each structure. The difficulty with static optimizations based on gradient algorithms is that the choice of the initial structure also determines the final configuration via the conjugate-gradient path—a crossing of saddle points leading to an eventually deeper minimum is excluded. A more extensive sampling of the configuration space may be achieved using a dynamical simulated annealing (DSA) strategy [62, 63]. Each simulated annealing run starts with a canonical molecular dynamics simulation at a high

temperature of 1500 K, i.e. far above the melting temperature of the cluster. During the high-temperature run, a large area of configuration space is sampled. The system was then gradually cooled down to room temperature before the final structural refinement using a static conjugate-gradient approach. If necessary, the quenching may be repeated starting from different high-temperature configurations.

3. Trends in binding energies, geometries, magnetic moments, and electronic properties as a function of cluster size

Figure 1 shows the cluster structures explored in this work. For the smallest clusters, the evident structural isomers extensively discussed in the literature were considered: dumbbell and triangle for dimers and trimers; square, rhombus, and tetrahedron for the tetramer; square pyramid and trigonal bipyramid for the pentamer; pentagonal pyramid and octahedron for the hexamer. These structures have been chosen as the starting configurations for the structural optimization. The optimizations have been performed without any symmetry constraint, i.e. distortions of the idealized geometries induced by a Jahn–Teller effect [52] or by a magnetostructural effect were not excluded during the structural optimization. For larger clusters, the choice of possible structural isomers is not so evident and, for the structures discussed previously in the literature, rather small binding energies (in comparison with slightly smaller or larger clusters) were calculated. In these cases we attempted to find energetically more favourable geometries via the dynamical simulated annealing (DSA) method described above. Indeed, for clusters with $N \geqslant 7$, DSA runs produced some surprising structures to be discussed in detail below.

For all starting geometries—those assumed *a priori* as well as the DSA-optimized structures—fixed-spin-moment calculations for possible magnetic isomers have been performed. For Pd_N clusters with $N \leqslant 7$, only non-magnetic and $M = 2\ \mu_B$ solutions have been considered (exploratory calculations show that high-spin isomers are unstable); for larger clusters, magnetic moments of up to $M = 8\ \mu_B$ have been admitted. A much wider range of magnetic moments must be considered for Rh_N clusters, with M up to $21\ \mu_B$.

Tables 1 and 2 list the binding energies (calculated relative to the spin-polarized atom), the average nearest neighbour bond lengths, the magnetic moments, and the energy gaps between the highest occupied molecular orbital (HOMO) and the lowest unoccupied molecular orbital (LUMO) for all structural and magnetic isomers of Pd_N and Rh_N clusters with $N = 2$–13. For each cluster size we have listed the starting structure used to initialize the static optimization, or the structure generated by a DSA run (these configurations are marked by an asterisk). As no symmetry constraint is imposed during the relaxation, the initial symmetry may be broken—in some cases symmetry breaking depends on the magnetic state of the cluster. The final relaxed configuration is characterized by its point group symmetry. For Pd we have systematically explored all possible magnetic isomers. For clusters with up to seven atoms these are the non-magnetic $S = 0$ and 1 ($M = 1\ \mu_B$) solutions; no solutions with higher moments exist. For larger Pd clusters, magnetic isomers with spin up to $S = 3$ are at least metastable. Rh_N clusters can carry even larger magnetic moments, and spin isomers with spins up to $S = 9$ ($M = 18\ \mu_B$) have been considered.

3.1. Binding energy

Figure 2 summarizes for the stable structural and magnetic isomers the variation of the binding energy, the average coordination number N_C, the nearest neighbour bond length d, the magnetic moment M, and the HOMO/LUMO gap with increasing cluster size. For $N \geqslant 3$ the binding energy increases essentially proportionally to $\sqrt{N_C}$, but this trend is clearly recognizable only

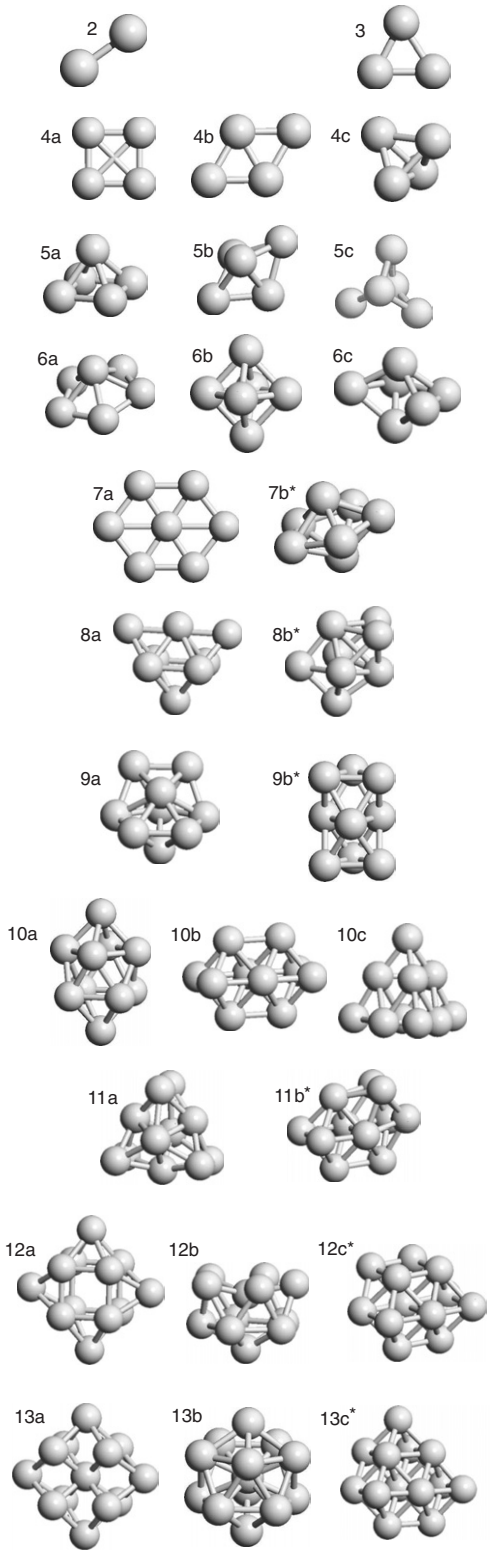

Figure 1. Final symmetric structures and structures produced by dynamical simulated annealing for clusters with 2–13 atoms: X_N with X = Pd or Rh and N = 2–13. Structures produced by dynamical simulated annealing are labelled with an asterisk. $N = 2$: dumbbell; $N = 3$: triangle; $N = 4$: square (4a), rhombus (4b), and tetrahedron (4c); $N = 5$: square pyramid (5a), trigonal bipyramid (TBP—5b), and flat trigonal bipyramid (5c); $N = 6$: pentagonal pyramid (6a), octahedron (6b), and incomplete pentagonal bipyramid (PBP) (6c); $N = 7$: centred hexagon (7a) and pentagonal bipyramid (PBP—7b*); $N = 8$: bicapped octahedron I (8a) and bicapped octahedron II (8b*); $N = 9$: bicapped PBP (9a) and double trigonal antiprism (9b*); $N = 10$: tetragonal antiprism (TAP) with capped square faces (10a), edge sharing double octahedra (10b), and trigonal pyramid (10c); $N = 11$: polytetrahedral cluster (11a) and edge sharing octahedra plus adatom (11b*); $N = 12$: cube with four capped surfaces (12a), incomplete icosahedron (12b), and cluster of octahedra (12c*); $N = 13$: capped cube with central atom (13a), centred icosahedron (13b), and cluster of octahedra (13c*). For details, see the text.

Table 1. Final structures (notation according to figure 1), point group symmetries PGS, total magnetic moments M (in μ_B), average coordination numbers N_C, average nearest neighbour distances d (in Å), HOMO–LUMO gaps E_g (in eV), and binding energies (in eV/atom) for structural and magnetic isomers of Pd_N clusters with $N = 2$–13. We use the Schönflies notation for the point group symmetry. An asterisk indicates that the antiferromagnetic or ferrimagnetic configuration breaks the PGS of the cluster geometry. The present results are compared with those of Barreteau *et al* [27] using an spd tight binding model and with *ab initio* DFT calculations of Kumar and Kawazoe [24]. The last two columns list the magnetic energy differences ΔE_{mag} for each structural isomer, and the structural energy difference ΔE_{struct} calculated for the respective magnetic ground state (in eV/atom).

							Binding energy				
N	Structure	PGS	M	N_C	d	E_g	This work	Ref. [27]	Ref. [24]	ΔE_{mag}	ΔE_{struct}
2	Dimer	$D_{\infty h}$	0	1	2.57	0.18	0.473			173	
		$D_{\infty h}$	2	1	2.48	0.32	0.646		0.611	—	
3	Triangle	C_{2v}	0	2	2.49	0.27	1.250	1.456		—	
		D_{3h}	2	2	2.52	0.00	1.250		1.203	—	
4a	Square	D_{4h}	0	2	2.60	1.04	1.234	1.463		251	
		D_{4h}	2	2	2.49	0.03	1.485			—	190
4b	Rhombus	D_{2h}	0	2.5	2.54	0.16	1.466			—	209
		D_{2h}	2	2.5	2.56	0.02	1.465			1	
4c	Tetrahedron	$S_4^\star$	0	3	2.61	0.12	1.654	1.781		21	
		T_d	2	3	2.61	0.00	1.675	1.857	1.628	—	—
5a	Square pyramid	C_{4v}	0	3.2	2.61	0.00	1.748			50	
		C_{4v}	2	3.2	2.61	0.19	1.798			—	7
5b	Trigonal bipyramid	$C_{2v}^\star$	0	3.6	2.64	0.00	1.760			45	
		D_{3h}	2	3.6	2.64	0.08	1.805		1.766	—	—
5c	Flat trigonal bipyramid	D_{3h}	0	2.4	2.55	0.00	1.671			58	
		D_{3h}	2	2.4	2.55	0.48	1.729			—	76
6a	Pentagonal pyramid	C_{1h}	0	3.3	2.63	0.10	1.756			21	
		C_{1h}	2	3.3	2.63	0.00	1.777			—	172
6b	Octahedron	D_{4h}	0	4	2.66	0.10	1.940	2.451	1.922	9	
		O_h	2	4	2.66	0.00	1.949	2.465	1.919	—	—
6c	Incomplete PBP	C_{2v}	0	4	2.67	0.24	1.897			10	
		C_{2v}	2	4	2.67	0.19	1.907			—	42
7a	Centred hexagon	D_{2h}	0	3.4	2.66	0.18	1.700			—	285
		D_{2h}	2	3.4	2.64	0.03	1.688			12	
7b*	Pentagonal bipyramid	C_{2v}	0	4.6	2.70	0.08	1.975	2.457	1.917	10	
		C_{2v}	2	4.6	2.70	0.07	1.985	2.490	1.953	—	—
8a	Bicapped octahedron I	C_{2v}	0	4.5	2.69	0.16	1.995			3	
		C_{2v}	2	4.5	2.69	0.13	1.994		2.036	4	
		C_{2v}	4	4.5	2.68	0.00	1.998			—	78
		C_{2v}	6	4.5	2.67	0.04	1.968			28	
8b*	Bicapped octahedron II	C_{2v}	0	4.5	2.67	0.17	2.058			18	
		C_{2v}	2	4.5	2.67	0.21	2.076			—	—
		C_{2v}	4	4.5	2.67	0.10	2.065			11	
		C_{2v}	6	4.5	2.67	0.07	1.995			81	
9a	Capped PBP	C_{1h}	0	4.9	2.68	0.05	2.108			21	
		C_{1h}	2	5.1	2.71	0.07	2.118			11	
		C_{1h}	4	5.1	2.71	0.10	2.129		2.094	—	10
9b*	Double trigonal antiprism	$C_{1h}^\star$	0	4.7	2.66	0.13	2.135			4	
		C_{2v}	2	4.7	2.66	0.00	2.139			—	—
		D_{3h}	4	4.7	2.67	0.05	2.134			5	

Table 1. (Continued.)

							Binding energy				
N	Structure	PGS	M	N_C	d	E_g	This work	Ref. [27]	Ref. [24]	ΔE_{mag}	ΔE_{struct}
10a	TAP with capped square faces	C_{4v}	0	4.8	2.68	0.13	2.131	2.529		9	
		C_{4v}	2	4.8	2.68	0.10	2.128	2.543		12	
		C_{4v}	4	4.8	2.68	0.09	2.140		2.119	—	45
10b	Edge sharing double octahedra	D_{2h}	2	5	2.68	0.07	2.175			10	
		D_{2h}	4	5	2.68	0.01	2.185			—	—
		D_{2h}	6	5	2.68	0.08	2.166			19	
10c	Trigonal pyramid	T	0	4.8	2.67	0.00	2.103			13	
		C_{2v}	2	4.8	2.67	0.22	2.116			—	69
		T	4	4.8	2.67	0.00	2.109			7	
		T	6	4.8	2.66	0.00	2.110			6	
11a	Polytetrahedral cluster	$C^{\star}_{2v}$	2	5.5	2.71	0.25	2.203			15	
		C_{2v}	4	5.5	2.71	0.08	2.214			4	
		C_{2v}	6	5.5	2.68	0.18	2.218			—	12
11b*	Edge sharing octahedra plus adatom	C_1	2	5.1	2.68	0.09	2.228			2	
		C_1	4	5.1	2.68	0.07	2.226			4	
		C_1	6	5.1	2.68	0.08	2.230			—	—
12a	Capped cube	D_{4h}	2	4.7	2.64	0.07	2.222			11	
		D_{4h}	4	4.7	2.64	0.17	2.233			—	41
		D_{4h}	6	4.7	2.64	0.00	2.207			26	
		D_{4h}	8	4.7	2.65	0.17	2.184			49	
12b	Incomplete icosahedron	C_{1h}	2	6	2.75	0.09	2.242	2.511		15	
		C_{1h}	4	6	2.74	0.03	2.250			7	
		C_{5v}	6	6	2.74	0.15	2.257		2.231	—	17
		C_{1h}	8	6	2.74	0.13	2.253			4	
12c*	Edge sharing octahedra plus two adatoms	C_{1h}	2	5.3	2.69	0.19	2.254			20	
		C_{1h}	4	5.3	2.69	0.07	2.259			15	
		C_{1h}	6	5.3	2.69	0.02	2.274			—	—
		C_{1h}	8	5.3	2.69	0.02	2.238			36	
13a	Capped cube with central atom	C_{2h}	2	5.5	2.73	0.14	2.278			7	
		D_{4h}	4	4.9	2.69	0.09	2.285			—	39
		D_{4h}	6	4.9	2.68	0.00	2.280			5	
		D_{4h}	8	4.9	2.70	0.11	2.266			19	
13b	Centred icosahedron	C_{2h}	0	6.5	2.75	0.05	2.273			31	
		C_{2h}	2	6.5	2.75	0.09	2.283	2.834		21	
		C_{2h}	4	6.5	2.75	0.00	2.287			17	
		I_h	6	6.5	2.75	0.01	2.285			19	
		I_h	8	6.5	2.75	0.06	2.304		2.290	—	20
13c*	Cluster of octahedra	C_{1h}	2	5.5	2.69	0.00	2.323			1	
		C_{1h}	4	5.5	2.69	0.04	2.321			3	
		C_{1h}	6	5.5	2.69	0.04	2.324			—	—
		C_{1h}	8	5.5	2.69	0.03	2.302			22	
Bulk		fcc	0	12	2.80		3.704		3.718		

on the basis of the geometries optimized using the dynamical simulated annealing approach. The smooth variation of the binding energy with the cluster size contrasts with the shell structure of the simple metal cluster [64–66]. For the cluster sizes considered here, the shell model based on a jellium approximation would predict an enhanced stability of the $N = 8$-atom cluster, which we find to be one of the difficult cases for structural optimization. For

Table 2. Final structures (notation according to figure 1), point group symmetries PGS, total magnetic moments M (in μ_B), average coordination numbers N_C, average nearest neighbour distances d (in Å), HOMO–LUMO gaps E_g (in eV), and binding energies (in eV/atom) for structural and magnetic isomers of Rh_N clusters with $N = 2$–13. We use the Schönflies notation for the point group symmetry. An asterisk indicates that the antiferromagnetic or ferrimagnetic configuration breaks the PGS of the cluster geometry. The present results are compared with those of Barreteau *et al* ([27], using an spd tight binding model), Reddy *et al* ([36], using an *ab initio* LCAO approach), Jinlong *et al* [13] and Wang and Ge [37] using an *ab initio* DFT approach. The last two columns list the magnetic energy differences ΔE_{mag} for each structural isomer, and the structural energy difference ΔE_{struct} calculated for the respective magnetic ground state (in eV/atom).

							Binding energy						
N	Structure	PGS	M	N_C	d	E_g	This work	Ref. [13]	Ref. [27]	Ref. [36]	Ref. [37]	ΔE_{mag}	ΔE_{struct}
2	Dimer	$D_{\infty h}{}^{\star}$	0	1	2.24	0.52	1.288		1.477			398	
		$D_{\infty h}$	2	1	2.18	0.10	1.387		1.488			299	
		$D_{\infty h}$	4	1	2.21	0.57	1.686	1.520		1.88	1.74	—	
3	Triangle	D_{3h}	1	2	2.38	0.35	2.234		2.034			74	
		D_{3h}	3	2	2.38	0.38	2.308	2.253	1.955	2.35	2.36	—	
		D_{3h}	5	2	2.43	0.08	2.280					28	
		D_{3h}	7	2	2.43	0.09	1.890					418	
4a	Square	D_{4h}	0	2	2.31	0.00	2.611	2.640	2.180			113	
		D_{4h}	2	2	2.32	0.11	2.662					62	
		D_{4h}	4	2	2.35	0.30	2.724	2.728	2.118	2.79	2.77	—	26
		D_{4h}	6	2	2.38	0.00	2.639					85	
4b	Rhombus	D_{2h}	0	2.5	2.42	0.24	2.399	2.655				156	
		D_{2h}	2	2.5	2.43	0.01	2.445					111	
		D_{2h}	4	2.5	2.43	0.10	2.508	2.733				47	
		D_{2h}	6	2.5	2.48	0.15	2.555					—	195
4c	Tetrahedron	T_d	0	3	2.45	0.60	2.750	2.950	2.370	2.91	2.81	—	—
		C_{1h}	2	3	2.48	0.15	2.677					73	
		S_4	4	3	2.51	0.13	2.693		2.369			57	
		T_d	6	3	2.52	0.08	2.646		2.293			104	
5a	Square	C_{4v}	3	3.2	2.47	0.07	3.006					22	
	pyramid	C_{4v}	5	3.2	2.49	0.43	3.028			3.11	3.08	—	—
		C_{4v}	7	3.2	2.51	0.26	3.017			3.13		11	
5b	Trigonal	D_{3h}	3	3.6	2.50	0.27	2.959	3.062				12	
	bipyramid	D_{3h}	5	3.6	2.52	0.13	2.948					23	
		D_{3h}	7	3.6	2.55	0.29	2.971					—	57
5c	Flat trigonal	D_{3h}	3	2.8	2.46	0.00	2.832					11	
	bipyramid	D_{3h}	5	2.8	2.42	0.00	2.807					36	
		D_{3h}	7	2.8	2.44	0.13	2.843					—	185
6a	Pentagonal	C_{1h}	2	3.3	2.49	0.38	2.944					63	
	pyramid	C_{1h}	4	3.3	2.51	0.31	2.985					22	
		$C^{\star}_{5v}$	6	3.3	2.50	0.02	2.995					12	
		$C^{\star}_{5v}$	8	3.3	2.51	0.38	3.007					—	197
6b	Octahedron	O_h	0	4	2.51	0.35	3.190	3.457	3.129	3.28		14	
		D_{4h}	2	4	2.52	0.04	3.153					51	
		D_{4h}	4	4	2.53	0.15	3.169					35	
		O_h	6	4	2.54	0.20	3.204	3.390	3.244	3.27	3.26	—	—
		D_{4h}	8	4	2.56	0.00	3.174		3.251			30	
6c	Incomplete PBP	C_{2v}	4	3.7	2.51	0.17	3.168					—	36
		C_{2v}	6	3.7	2.51	0.13	3.123					45	
		C_{2v}	8	3.7	2.54	0.04	3.028					140	

Table 2. (Continued.)

							Binding energy						
N	Structure	PGS	M	N_C	d	E_g	This work	Ref. [13]	Ref. [27]	Ref. [36]	Ref. [37]	ΔE_{mag}	ΔE_{struct}
7a	Centred	D_{2h}	5	3.4	2.47	0.35	2.888				2.96	39	
	hexagon	D_{2h}	7	3.4	2.49	0.08	2.889					38	
		D_{2h}	9	3.4	2.51	0.02	2.896					31	
		D_{2h}	11	3.4	2.52	0.12	2.922					5	
		D_{2h}	13	3.4	2.52	0.03	2.927					—	377
		D_{2h}	15	3.4	2.54	0.00	2.795					31	
7b*	Pentagonal	$C^{\star}_{5h}$	5	4.6	2.57	0.17	3.180					124	
	bipyramid	C_{2v}	7	4.6	2.58	0.00	3.213					91	
		C_{2v}	9	4.6	2.58	0.00	3.259	3.433	3.246	3.33		45	
		C_{2v}	11	4.6	2.59	0.26	3.285					19	
		$C^{\star}_{5h}$	13	4.6	2.58	0.52	3.304					—	—
8a	Bicapped	C_{2v}	0	4.5	2.53	0.00	3.317					12	
	octahedron I	C_{2v}	2	4.5	2.54	0.04	3.327					2	
		C_{2v}	4	4.5	2.55	0.15	3.323					6	
		C_{2v}	6	4.5	2.54	0.31	3.325					4	
		C_{2v}	8	4.5	2.55	0.10	3.329					—	11
8b*	Bicapped	C_{2v}	4	4.5	2.55	0.10	3.388					48	
	octahedron II	C_{2v}	6	4.5	2.55	0.27	3.401					29	
		C_{2v}	8	4.5	2.55	0.00	3.426					4	
		C_{2v}	10	4.5	2.56	0.00	3.430					—	—
9a	Capped PBP	C_{1h}	9	5.1	2.59	0.17	3.461					12	
		C_{1h}	11	5.1	2.60	0.17	3.473					—	25
		C_{1h}	13	5.1	2.60	0.20	3.471					2	
9b*	Double trigonal	C_1	9	4.7	2.56	0.05	3.479					19	
	antiprism	D_{3h}	11	4.7	2.56	0.23	3.498					—	—
		D_{3h}	13	4.7	2.56	0.20	3.488					10	
10a	TAP with capped	C_{4v}	0	4.8	2.55	0.00	3.574	3.762	3.409			141	
	square faces	C_{4v}	6	4.8	2.55	0.19	3.572	3.773				101	
		C_{4v}	8	4.8	2.55	0.00	3.553					81	
		C_{4v}	10	4.8	2.55	0.00	3.573		3.442			61	
		C_{4v}	12	4.8	2.55	0.00	3.606		3.438			28	
		C_{4v}	14	4.8	2.56	0.00	3.634	3.755				—	—
		C_{4v}	16	4.8	2.57	0.00	3.618					16	
10b	Edge sharing	D_{2h}	10	5	2.56	0.18	3.600					7	
	double octahedra	D_{2h}	12	5	2.57	0.19	3.607					—	27
		D_{2h}	14	5	2.58	0.04	3.597					10	
		D_{2h}	16	5	2.59	0.13	3.604					3	
10c	Trigonal pyramid	C_{1h}	0	4.8	2.53	0.09	3.551					15	
		C_{1h}	2	4.8	2.54	0.21	3.566					—	68
		C_{1h}	4	4.8	2.54	0.28	3.545					21	
		C_{1h}	6	4.8	2.55	0.00	3.518					48	
11a	Polytetrahedral	C_{2v}	3	4.9	2.54	0.11	3.658					9	
	cluster	C_{2v}	5	4.9	2.55	0.14	3.667					—	7
		C_{2v}	7	4.9	2.55	0.16	3.666					1	
		C_{2v}	9	4.9	2.55	0.15	3.659					8	
		C_{2v}	11	4.9	2.56	0.10	3.653					14	
		C_{2v}	13	4.9	2.57	0.07	3.654					13	
11b*	Edge sharing	C_1	5	5.1	2.56	0.20	3.648					26	
	octahedra plus	C_1	7	5.1	2.56	0.18	3.654					20	
	adatom	C_1	9	5.1	2.57	0.12	3.662					12	

Table 2. (Continued.)

							Binding energy						
N	Structure	PGS	M	N_C	d	E_g	This work	Ref. [13]	Ref. [27]	Ref. [36]	Ref. [37]	ΔE_{mag}	ΔE_{struct}
		C_1	11	5.1	2.57	0.11	3.667					7	
		C_1	13	5.1	2.58	0.20	3.674					—	—
12a	Capped cube	C_{2h}	12	4.7	2.55	0.06	3.629					22	
		D_{4h}	14	4.7	2.54	0.23	3.654					—	60
		D_{4h}	16	4.7	2.55	0.25	3.651					3	
12b	Incomplete	C_{1h}	8	6	2.64	0.18	3.646					35	
	icosahedron	C_{1h}	10	6	2.63	0.04	3.641					40	
		C_{1h}	12	6	2.63	0.16	3.654					27	
		C_{1h}	14	6	2.63	0.15	3.649					32	
		C_{1h}	16	6	2.64	0.15	3.662					19	
		C_{1h}	18	6	2.64	0.16	3.681					—	33
12c*	Edge sharing	C_{1h}	12	5.3	2.59	0.00	3.705					9	
	octahedra plus	C_{1h}	14	5.3	2.59	0.13	3.710					4	
	two adatoms	C_{1h}	16	5.3	2.59	0.16	3.714					—	—
		C_{1h}	18	5.3	2.60	0.09	3.713					1	
13a	Capped cube	$D^{\star}_{4h}$	5	4.3	2.52	0.12	3.691					—	99
	with central atom	C_{2h}	7	4.9	2.58	0.05	3.685					6	
		D_{4h}	9	5.5	2.63	0.12	3.690					1	
		C_{2h}	11	5.2	2.58	0.17	3.685					6	
13b	Centred	C_{2h}	7	7	2.64	0.18	3.692	3.955				53	
	icosahedron	I_h	15	7	2.65	0.31	3.739	4.012	3.847			6	
		I_h	17	7	2.65	0.26	3.742				3.79	3	
		C_{2h}	21	7	2.67	0.18	3.745	3.985				—	45
13c*	Cluster of	C_{1h}	13	5.5	2.59	0.01	3.788					2	
	octahedra	C_{1h}	15	5.5	2.59	0.14	3.790					—	—
		C_{1h}	17	5.5	2.60	0.06	3.779					11	
Bulk		fcc	0	12	2.72		5.744						

transition metal clusters, a tight binding model seems to be a more appropriate zeroth-order approximation. Assuming that the hopping integral h is the same for between all neighbouring atoms, tight binding theory predicts [67] the binding energy in a condensed system to be proportional to the hopping integral and to the square root of the average coordination number N_C, $E_{bind} = \sqrt{N_C}|h|$. We find that the optimized binding energies follow this simple relation rather well (see figure 2). Extrapolation of the trend derived from the small clusters to the face-centred cubic crystal with $N_C = 12$ gives for Pd a binding energy of 3.43 eV/atom, in reasonable agreement with a calculated cohesive energy of 3.70 eV/atom. Only for the smallest Pd clusters is an excess stability of the tetrahedron and the octahedron (as measured by the difference of its binding energy from the average binding energies with one atom more or less) recognizable, and the trigonal and pentagonal bipyramids of the $N = 5$ and 7 clusters have a binding energy that is lower than the average binding energies of the tetrahedron and the octahedron, and of the octahedron and the double trigonal antiprism (for the $N = 9$ cluster), respectively. For larger N no clusters with particular stability can be identified. For Rh clusters the binding energy is a convex function of the cluster size even for the smallest clusters; neither the tetrahedron nor the octahedron excel by an enhanced stability compared to their neighbours. For the tetrahedron this is eventually related to a frustration of magnetism (for details, see below).

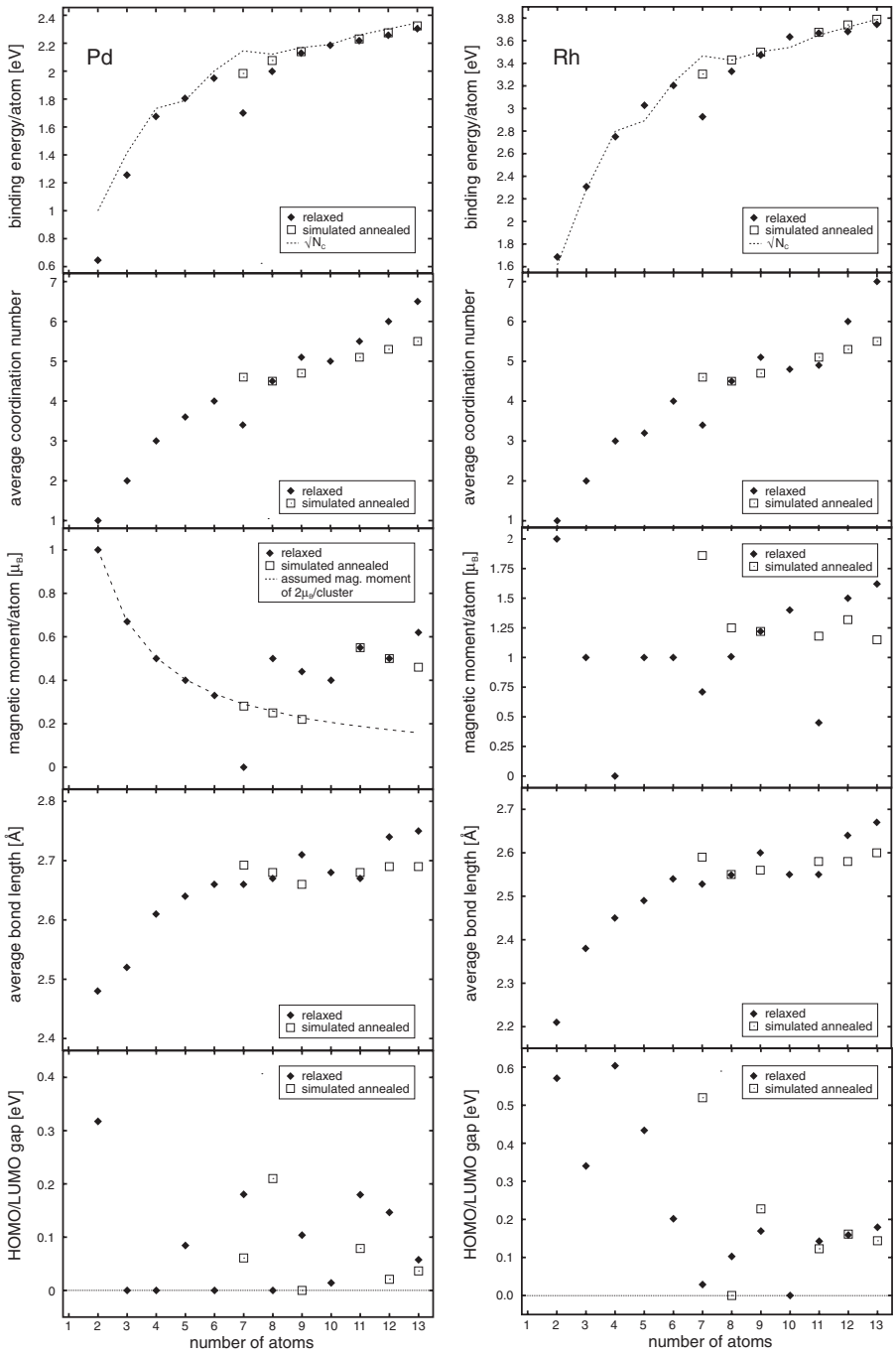

Figure 2. Binding energy, average coordination number, magnetic moment/atom, average bond length, and HOMO/LUMO gap for energetically preferred Pd_N and Rh_N clusters with $N = 2$–13. The filled rhombi represent the stable structural and magnetic isomers obtained by static relaxation calculations, whereas the open squares show the results of simulated annealing. The dashed lines in the uppermost panels display the variation of the binding energy with the square root of the average coordination number, as expected from simple tight binding arguments; cf text.

Tables 1 and 2 report the same information (plus the magnetic and structural energy differences) for all structural and magnetic isomers considered in our study. For comparison we have also listed binding energies from calculations published in the literature. For Pd_N clusters, we refer to the work of Barreteau *et al* [27] based on tight binding (TB) techniques and to the calculations of Kumar and Kawazoe [24], also using VASP. Due to a less stringent setting of the computational parameters, the binding energies given by Kumar and Kawazoe are lower by about 20–30 meV than our values, but the structural energy differences are in better agreement. The important difference between our work and that of Kumar and Kawazoe is that with their restricted set of starting structures and symmetry-constrained relaxations, the stable configurations for larger clusters could not be identified. Much larger differences are found relative to the TB work of Barreteau *et al*. Their binding energies are much larger and—more importantly—the TB calculations tend to grossly overestimate the magnetic energy differences, while underestimating the structural energy difference. Take for example the Pd_4 cluster: for the structural energy difference between the $S = 0$ isomers of the square and the tetrahedron we find a value of 0.420 eV/atom, compared to the TB result of 0.318 eV/atom; for the magnetic energy differences between the $S = 0$ and 1 isomers of the tetrahedron, the values are 22 meV/atom (present work) and 76 meV/atom (TB result). For Rh_N clusters we have chosen a larger database for comparison, including again the TB work of Barreteau *et al* [27], the work of Reddy *et al* [31] based on an *ab initio* LCAO technique, and the work of Jinlong *et al* [13] and of Wang and Ge [37]. Wang and Ge also used our VASP software; their binding energies differ from ours by a constant increment of 0.06 eV/atom to be attributed to a different choice of reference state for the isolated Rh atom. Interestingly, the TB calculations [27] now produce significantly smaller binding energies than the *ab initio* DFT calculations, emphasizing the uncertainties in determining the TB parameters. The older work of Jinlong *et al* [13] is based on the local spin density approximation and does not include gradient corrections, but this is one of the few papers looking into the relative stability of different spin isomers. For the smaller clusters, agreement with our predictions for the most stable isomers is good, but for the octahedron where we predict a stable $S = 3$ state, the LSDA calculations find a non-magnetic ground state. Such differences are not unexpected, as the gradient corrections tend to stabilize magnetism in solids as well as in clusters. A similar preference for a low-spin $S = 3$ solution instead of our $S = 7$ state is found for the Rh_{10} cluster and for the Rh_{13} icosahedron. For the Rh_{12} cluster in an icosahedral structure with a vacant centre, Jinlong *et al* also report a low-spin ($S = 4$) state, whereas we find the empty icosahedron to be structurally unstable. A vacant site is more easily accommodated at an outer vortex of the icosahedron at its centre. This configuration breaks the icosahedral symmetry. This result demonstrates the importance of an unconstrained structural optimization.

3.2. Cluster geometry

Optimization of the cluster geometry has been performed without any symmetry constraints. Structural distortions may be driven by a different mechanism: a genuine instability of the assumed structure under the action of the interatomic forces, a Jahn–Teller mechanism if partially occupied eigenstates exist, or via magnetostructural effects. To monitor structure changes during the relaxation, we list in tables 1 and 2 the chosen starting structure together with the point group symmetry of the final relaxed configuration.

A striking example of a magnetically induced distortion is observed, e.g., for a Pd_4 tetrahedron: the magnetic $S = 0$ isomer adopts an antiferromagnetic configuration with local moments of $\pm 0.26\ \mu_B$; the symmetry is lowered to S_4 (we use the Schönflies notation for the point group symmetry). The ground state is the $S = 1$ isomer which conserves the

full tetrahedral T_d symmetry. An even more complex situation is found for the Rh_4 clusters where the non-magnetic $S = 0$ (ground state) and the high-spin $S = 3$ isomers conserve the full tetrahedral symmetry, whereas at intermediate magnetic moments ($S = 1$ and 2) the symmetry is reduced. For the $S = 1$ state the geometric and magnetic symmetry is C_{1h}. Three Rh atoms carry the magnetic moments of $\sim$0.64 μ_B, whereas the fourth atom has a very low moment of only 0.09 μ_B. The magnetic moments appear to be compatible with a threefold axis through the low-spin state, but the trigonal symmetry is broken by the distortion of the triangular face opposite to this site, with edge lengths of 2.73 Å and two times 2.43 Å (for details see below and supporting material). The symmetry of the $S = 2$ isomer is reduced to S_4 (as for the non-magnetic Pd_4 tetrahedron) with two long edges of 2.71 Å and four short edges of 2.40 Å. Similar magnetostructural effects are detected also in larger clusters.

Geometry optimization of the larger clusters offers some surprises: the stable structures of the clusters with $N = 11$, 12, and 13 are not based on icosahedral or cubo-octahedral motifs as frequently assumed in the literature, but can be described as clusters of octahedra with adatoms (for details see below). These results contradict simulations [68] based on semi-empirical many-atom potentials of the embedded-atom type which predict a stabilization of near crystalline motifs only at much larger cluster sizes. The results of the structure optimizations also serve as a warning against overstretching of simple tight binding arguments: for $N = 13$ the stable structure is neither a centred icosahedron ($N_C = 6.46$), nor a centred cube with capping atoms ($N_C = 5.54$) or the cubo-octahedron ($N_C = 4.61$), but a polyoctahedral cluster with $N_C = 5.54$ representing the optimal compromise between maximizing the number of nearest neighbour bonds (as in the icosahedron) and the building of symmetry-adapted hybrid orbitals based on s and d states. The cubo-octahedron is even found to be completely unstable and relaxed for both Pd and Rh to an eventually distorted centred cube with four capped square faces. Again magnetostructural effects are important. For Pd_{13}, the cluster geometry is compatible with D_{4h} symmetry for all spin isomers, but the low-spin $S = 1$ isomer has a completely asymmetric magnetic configuration. For the Rh_{13} cluster, only the $S = 9/2$ isomer has full C_{4v} symmetry in its geometric and magnetic structure. The $S = 5/2$ isomer has a geometric structure compatible with C_{4v}, but slight differences in the magnetic moments lower the symmetry of the magnetic structure. For the $S = 7/2$ and the $S = 11/2$ isomers, the symmetry is reduced to C_{2h}—the driving factors in the symmetry breaking are significant differences in magnetic moment between two pairs of capping atoms (see supporting information for details).

The average bond lengths in the smaller clusters are considerably shorter than the equilibrium nearest neighbour distance in the bulk metals (Pd: $d = 2.80$ Å, Rh: $d = 2.715$ Å) and increase slowly with cluster size. For our largest clusters, the average nearest neighbour distance reaches about 95% of the bulk value. In general, the geometries optimized by dynamical simulated annealing are more compact (shorter bond length) than the highly symmetric geometries generally assumed in the literature.

3.3. Magnetic moment

For the magnetic moment, we find a clear trend with increasing cluster size for the Pd clusters: the isolated Pd atom is non-magnetic; for all clusters up to $N = 9$ the stable magnetic isomer is $S = 1$; for $N = 10$ the magnetic ground state is $S = 2$; and for $N \geqslant 11$ the stable isomer is $S = 3$. The low-spin isomers are metastable for the larger clusters. The magnetic energy differences become very small, of the order of a few meV/atom. Hence room temperature experiments will always average over all possible spin isomers. Magnetostructural effects are evident—different geometries also lead in most cases to different magnetic ground states (details to be discussed below).

For Rh clusters, the situation is more complex. Due to its open-shell configuration an isolated Rh atom has a magnetic moment of 3 μ_B in its DFT ground state. For the three smallest clusters, the magnetic moment per atom of the most stable structural and magnetic isomers (dimer, triangle, and tetrahedron) decreases linearly from 2 μ_B/atom in the dimer to 1 μ_B/atom in the trimer and to zero for the tetramer. The Rh_4 tetrahedron is hence the smallest non-magnetic Rh cluster. For $N = 5$–13, the magnetic moment of the most stable isomer fluctuates around 1 μ_B/atom. However, magnetic energy differences are rather small, so the measured magnetic moment must be compared with a weighted average over the thermodynamically accessible spin isomers. If this is done (for details see below), we find reasonable agreement with the experimental estimates of Cox *et al* [10, 11].

3.4. Electronic properties

The HOMO/LUMO gap generally decreases with increasing cluster size, but due to a smaller exchange splitting, this decrease is much faster for Pd_N clusters where the gap is smaller than 0.1 eV for all $N \geqslant 8$ clusters and almost vanishes for the stable $N = 9$, 10, and 12 isomers. However, one should remember the tendency of DFT to systematically underestimate the gap width. A partially occupied HOMO is found for the magnetic ground state ($S = 1$) of triangular Pd_3 and tetrahedral Pd_4, whereas for the antiferromagnetic ($S = 0$) isomers, where magnetostructural effects break the symmetry, a small HOMO/LUMO gap exists (see also figure 3). For a partially occupied HOMO, a Jahn–Teller distortion is expected, but this cannot be produced by DFT calculations (see below for more details). Similarly, the octahedral Pd_6 cluster has a partially occupied HOMO for the fully symmetric (O_h) $S = 1$ isomers, whereas for the non-magnetic isomers the symmetry is reduced to D_{4h} and a small gap is created. A partially occupied HOMO exists also for the metastable structural isomer of Pd_8, but not for the structure created by DSA—although both have C_{2v} symmetry. Vice versa, for Pd_9 the double trigonal antiprism created by DSA has a partially occupied HOMO in the stable $S = 1$ isomer—in spite of a reduced symmetry (C_{1h}), whereas the only slightly less stable $S = 2$ isomer ($\Delta E_{mag} = 5$ meV) with full D_{3h} symmetry has a small gap.

For Rh clusters partially occupied HOMOs are found for the high-spin isomers of Rh_8 (bicapped octahedron) and of Rh_{10} (tetragonal antiprism with capped square faces).

4. Structure, magnetic, and electronic properties of Pd_N and Rh_N clusters

4.1. Pd_2 and Rh_2

For the Pd dimer, the binding energy amounts to 0.646 eV/atom and the total magnetic moment equals 2 μ_B (i.e. 1 μ_B/atom). In comparison with bulk Pd ($d = 2.80$ Å), the bond length of the dimer is contracted to 2.48 Å. As can be seen from the electronic eigenvalue spectrum represented in figure 3, the HOMO/LUMO gap has a value of $E_g = 0.3174$ eV. In agreement with the findings of Kumar *et al* [24], we find sp–d hybridization to lead to a full occupation of the 4d majority spin states while the 4d minority spin states are depleted. The bond length and magnetic moment are in good agreement with other theoretical studies, e.g., Kumar *et al* [24], Efremenko *et al* [26], Moseler *et al* [23], and Lee *et al* [19]. In disagreement with our work, Barreteau *et al* [27], using an spd tight binding model, found a non-magnetic solution to be the ground state of the Pd dimer. The experimental binding energies reported in the literature [69, 70] for the Pd_2 dimer scatter between 0.37 and 0.57 eV/atom. High-level quantum chemistry calculations [16] also predict a triplet ground state with the identical bond length of 2.48 Å, but a lower binding energy of 0.43 eV/atom in better agreement with

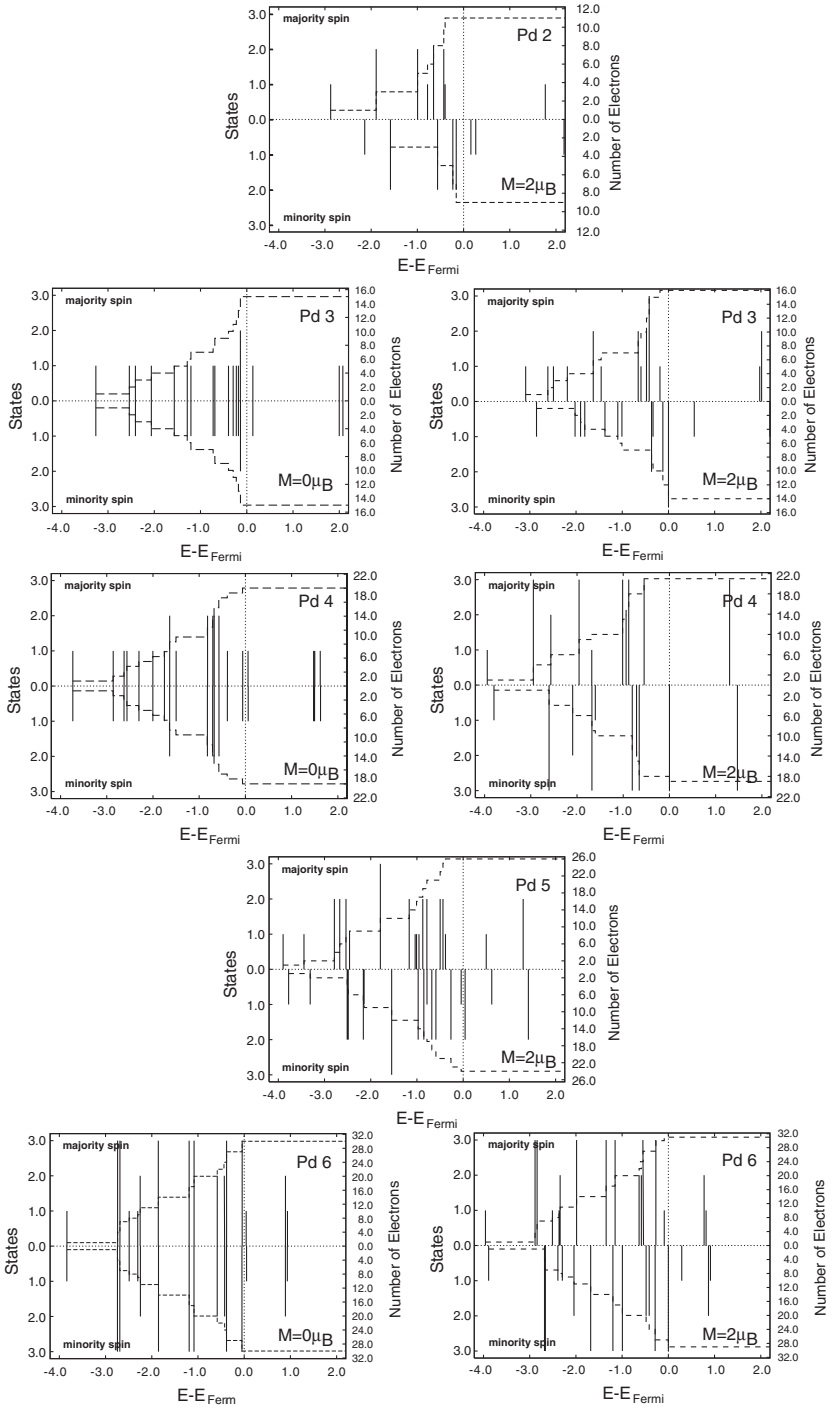

Figure 3. Total spin-polarized differential (left scale) and integrated (right scale) density of states for Pd_2, Pd_3, tetrahedral Pd_4, trigonal–bipyramidal Pd_5, and octahedral Pd_6, calculated for different spin isomers.

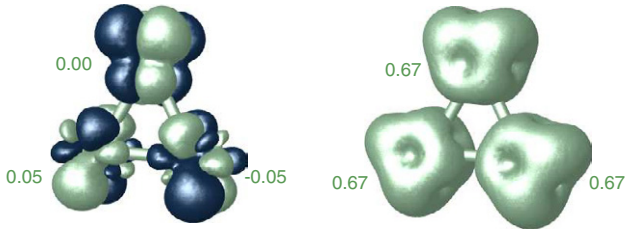

Figure 4. Isosurfaces of the magnetization densities for $M = 0\ \mu_B$ (left) and $M = 2\ \mu_B$ (right) for the Pd_3 triangle. Dark blue surfaces surround regions of negative magnetization, green surfaces regions of positive magnetization.

experiment. Calculations [20] based on hybrid functionals mixing DFT and exact (Hartree–Fock) exchange predict a substantially larger bond length of 2.53 Å and a binding energy of 0.48 eV.

The magnetic ground state of the Rh dimer we found to be the $M = 4\ \mu_B$ ($2\ \mu_B$/atom) spin isomer with a binding energy of 1.686 eV/atom. Its bond length amounts to 2.21 Å (strongly contracted compared to the Rh–Rh nearest neighbour distance of 2.715 Å in bulk Rh). The magnetic moment of $2\ \mu_B$/atom is in good agreement with other theoretical studies [13, 34–37] and with experiment [71]. The low-spin isomers have a much higher energy; the $S = 0$ configuration is weakly antiferromagnetic with local moments of $\pm 0.14\ \mu_B$ and a bond length increased by 0.03 Å. In contrast to the good agreement for the spin multiplicity of the ground state, the values for the binding energy of the Rh dimer found in the literature scatter widely. Gingerich and Cocke [71] report an experimental binding energy of 1.46 eV/atom for a Rh_2 dimer. The comparison between theory and experiment for both dimers shows that even in the GGA the overbinding tendency characteristic for density functional techniques is not completely removed.

4.2. Pd_3 and Rh_3

For the $N = 3$ clusters, the triangular configuration has been shown to have a much lower energy than the linear chain. However, the HOMO of the triangular Pd_3 cluster in its $M = 2\ \mu_B$ ground state is degenerate and partially occupied, so a Jahn–Teller distortion is expected. The degeneracy of the HOMO is a consequence of the exchange splitting. In the $S = 0$ isomer of a triangular Pd_3 cluster the symmetry is lowered to C_{2v} (although the difference in bond length is only 0.01 Å) and the magnetization densities (see figure 4) show a non-vanishing spin polarization of the occupied eigenstates (although integration over atomic spheres leads to almost vanishing local moments). Due to the mirror symmetry, occupation by spin-up and spin-down electrons is interchanged on sites 1 and 2, and a similar symmetry is also found on site 3.

In the $S = 1$ isomer, with full D_{3h} symmetry, the non-degenerate state is shifted below the Fermi level, and the now degenerate threefold minority HOMO is occupied by only two electrons (see figure 4). The theorem of Jahn and Teller [52] states that if the HOMO is degenerate and partially occupied, a structural distortion that breaks the symmetry will remove the degeneracy and lower the total energy. A $D_{3h} \rightarrow C_{2v}$ distortion of the equilateral triangle would lift the degeneracy of this state, which means the highly symmetric D_{3h} equilateral triangular geometry of the Pd_3 cluster should be unstable against a Jahn–Teller distortion. Our calculations, however, did not show this instability and the equilateral triangle was found to be the energetically most stable Pd_3 isomer. The stability against Jahn–Teller distortions is

an artefact introduced by the way exchange and correlation are commonly approximated in DFT. In the conventional DFT the electron density distribution $n(\vec{r})$ is represented by that of a single-determinant ground state of non-interacting electrons in an external potential $v(\vec{r})$—such systems are called pure-state v-representable (P-VR). Most physical systems are P-VR. However, there are also densities which can be represented only by a weighted sum of the densities of several degenerate single-determinant ground states. These systems are called ensemble v-representable (E-VR). Prominent examples are the C_2 molecule and the $H_2 + H_2$ reaction [72], but also the triangle cluster with a degenerate ground state. Formal Kohn–Sham equations for E-VR systems have been developed by Ullrich and Kohn [53], but so far this generalized Kohn–Sham equation has been used only for very simple systems (e.g. the Be_2 dimer) as an *ex post* correction to a self-consistent Kohn–Sham calculation with a conventional functional. That the stability of the equilateral Pd_3 triangle is a DFT artefact is also made plausible by the work of Valerio and Toulhoat [20] and of Balasubramanian [16], which shows Pd_3 clusters to be stable against Jahn–Teller distortions at the GGA level, but to undergo a distortion when a hybrid functional mixing DFT and exact exchange is used or if the calculation is performed at the Hartree–Fock + configuration interaction (HF-CI) level.

In the case of the Rh_3 equilateral triangle (D_{3h}) we compared four spin isomers with magnetic moments of 1, 3, 5, and 7 μ_B. All spin isomers are ferromagnetic and conserve the D_{3h} symmetry of the equilateral triangle; all have a non-zero HOMO/LUMO gap (see table 2). In agreement with the results of Nayak *et al* [34] and Wang and Ge [37], but in disagreement with Chien *et al* [35] and Reddy *et al* [36], we found the $M = 3\ \mu_B$ isomer with a binding energy of 2.308 eV/atom and a bond length of $d = 2.38$ Å to be the ground state. The bond length increases slightly for the metastable high-spin isomers. Chien *et al* found that within the LDA the ground state has D_{3h} symmetry and a magnetic moment of $M = 3\ \mu_B$, whereas GGA calculations predicted a C_{2v} symmetry for an $S = 5/2$ isomer. Reddy *et al* also found the $S = 5/2$ isomer in an isosceles triangle to be slightly lower in energy.

4.3. Pd_4 and Rh_4

For the Pd_4 cluster we compared two planar structures, the square (D_{4h}) and the rhombus (C_{2h}), and the smallest three-dimensional cluster, the tetrahedron (T_d) (see figure 1). Table 1 lists the binding energy/atom for the non-magnetic and 2 μ_B spin isomers of these three Pd_4 clusters. In the case of the square and tetrahedral geometries the magnetic solution is energetically preferred over the non-magnetic solutions by 0.251 and 0.021 eV/atom, respectively. In the case of the rhombus the non-magnetic and magnetic spin isomers are almost energetically degenerate (the difference in the free energy is 0.001 eV/atom). Bond lengths and HOMO–LUMO gaps for these isomers are listed in table 1. The energetically most favourable structural and spin isomer is the tetrahedral Pd_4 cluster with an average bond length of 2.61 Å, a total magnetic moment of 2 μ_B (0.5 μ_B/atom), and a binding energy of 1.675 eV/atom, which is in good agreement with the results of previous work [17, 23, 27]. The HOMO (minority spin) of the tetrahedral Pd_4 cluster is threefold degenerate and partially occupied by only one electron (see figure 3). In disagreement with Kumar *et al* [24] and despite the similarity of our theoretical approach and the one used these authors, our calculations did not show tetrahedral Pd_4 to undergo a Jahn–Teller distortion. However, Dai *et al* [17], who studied the Pd_4 clusters at a considerably higher level of theory, using a complete active space self-consistent field (CASSCF) approach followed by a multi-reference singles + doubles configuration interaction (MRSDCI), also consider the ground state of Pd_4 to be an undistorted tetrahedron. The tetrahedral Pd_4 cluster is the simplest example of a magnetostructural effect. The antiferromagnetic $S = 0$ isomer has local magnetic moments of $\pm 0.26\ \mu_B$ on pairs of Pd atoms occupying opposite edges of a

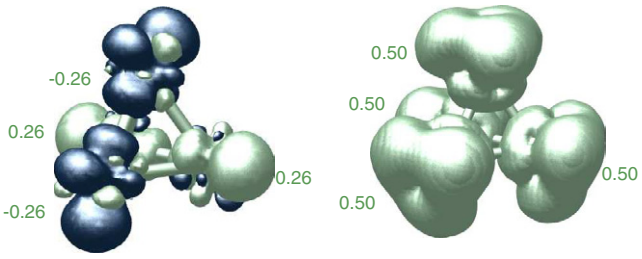

Figure 5. Isosurface plots of the magnetization densities and local magnetic moments (in μ_B) of the $S = 0$ (left) and $S = 1$ (right) spin isomers of Pd_4. Dark surfaces surround regions of negative magnetization, light surfaces regions of positive magnetization. For the $S = 0$ isomer the symmetry is lowered from T_d to S_4.

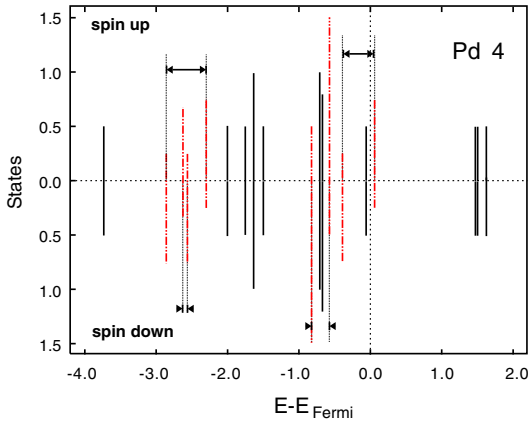

Figure 6. Local density of states at sites 1 and 4 of the antiferromagnetic $S = 0$ Pd_4 tetrahedron, carrying negative moments of $-0.26\ \mu_B$. Solid (black) lines represent spin-degenerate states which are distributed over all atoms. The dashed (red) lines represent spin-polarized states; the magnitude of the exchange splitting is indicated by the horizontal arrows. For one of these states, the exchange splitting pushes the spin-up component above the Fermi level. The negative magnetization densities shown in figure 5 represent these states. For the states localized predominantly at atoms Nos 2 and 3, the occupation of the spin-up and spin-down components is reversed; hence these sites carry a magnetic moment of $0.26\ \mu_B$. See the text.

distorted tetrahedron (see figure 5). The symmetry is lowered from T_d to S_4, with interatomic distances of 2.56 Å between ferromagnetically occupied Pd atoms and 2.63 Å between antiferromagnetically coupled pairs. The magnetization densities of both spin isomers are shown in figure 5.

It is interesting to observe that in the $S = 0$ isomer, the magnetization densities around atoms with like moments extend along the connecting line, while the overlap is minimized between atoms with opposite moments. An analysis of the local DOS projected onto a pair of atoms with like moments (see figure 6) demonstrates the absence of exchange splitting on most eigenstates which show an equal occupation of spin-up and spin-down states, while for certain strong coupling eigenstates a splitting of up to 0.56 eV is calculated. These states are occupied preferentially by one spin component on one pair of atoms, while on the pair with opposite magnetic moments the preferred spin orientation is reversed so that the total DOS (see figure 3) does not show any spin polarization. The HOMO is a non-spin-polarized eigenstate, while the LUMO is a spin-split state whose counterpart lies about 0.4 eV below the Fermi

Figure 7. Local magnetic moments (in μ_B) and isosurface plots of the magnetization densities of the $S = 1$ (left), $S = 2$ (centre), and $S = 3$ (right) spin isomers of Rh_4. Dark surfaces surround regions of negative magnetization, light surfaces regions of positive magnetization. For the $S = 1$ and 2 isomers the symmetry is lowered from T_d to C_{1h} and S_4, respectively. See the text.

energy (the exchange splitting of these states is 0.45 eV). The magnetization density of this antiferromagnetic $S = 0$ configuration shown in figure 5 is determined by this spin-polarized eigenstate. It should be noted that the structural distortion of the non-magnetic isomer is driven not by a Jahn–Teller effect, but by the imposed constraint $S = 0$ which cannot be met while tetrahedral symmetry is conserved. We also note that due to a small magnetic energy difference, the distorted $S = 0$ isomer will be observed with a non-negligible probability at finite temperatures.

In the case of Rh_4 we studied the same structural isomers as were mentioned above for Pd_4. As can be seen in table 2 we found the non-magnetic (undistorted) tetrahedron, with a binding energy of 2.750 eV/atom, to be the ground state of Rh_4. It is energetically more favourable than its own 2 μ_B spin isomer ($E_B = 2.677$ eV/atom), and the most stable spin isomers of the square ($E_B = 2.724$ eV/atom, 4 μ_B) and the rhombus ($E_B = 2.555$ eV/atom, 6 μ_B). The analysis of the magnetization densities and of the local DOS demonstrates that, in contrast to that for Pd_4, the $S = 0$ isomer of Rh_4 is genuinely non-magnetic. This result is in good agreement with those published in the literature [13, 27, 34–36, 73]. For the square and the rhombus, all spin isomers conserve the full symmetry (D_{4h} and D_{2h}, respectively). While for the square, the $S = 0$ isomer is non-magnetic and all magnetic states ferromagnetic, the low-spin isomers of the rhombus ($S = 0$ and 1) are antiferromagnetic with pairs of parallel moments coupled along the short and long diagonals. The energetically more favourable high-spin isomers ($S = 2$ and 3) are ferromagnetic, with almost equal local moments on all four sites.

Like for the Pd_4 tetrahedron, we note a very interesting magnetostructural effect: while for the paramagnetic and for the high-spin $S = 3$ isomers, both the geometric and the magnetic structures show full tetrahedral (T_d) symmetry, for the $S = 1$ and 2 isomers the symmetry is reduced to C_{1h} and S_4, respectively, with differences in the interatomic distances of up to 0.33 Å. For the $S = 1$ isomer the magnetic symmetry is almost that of a trigonal pyramid, with an almost non-magnetic atom ($M_1 = 0.09$ μ_B) at the vertex and three almost equal (0.64, 0.64 and 0.63 μ_B) moments at the corners of the base (the magnetization densities for the $S = 1$–3 isomers are shown in figure 7), but the geometric distortion of the base (two edges measure 2.43 Å, one measures 2.71 Å) lowers the symmetry to C_{1h}. For the $S = 2$ isomer, all local magnetic moments are almost equal ($M = 1.00 \pm 0.01$ μ_B), but the symmetry of the cluster geometry is only S_4, with two long (2.73 Å) and four short edges (2.40 Å). The structural distortion also influences the magnetic energy differences (see table 2), which increase first with increasing magnetic moment, but decrease again for the $S = 2$ isomer—evidently for the low-symmetry $S = 1$ isomer, the energy for the structural distortion adds to the magnetic energy difference. The magnetization-induced changes in the cluster geometry are also reflected in the electronic spectrum, as demonstrated in figure 8. While for the $S = 0$ and 3 isomers with

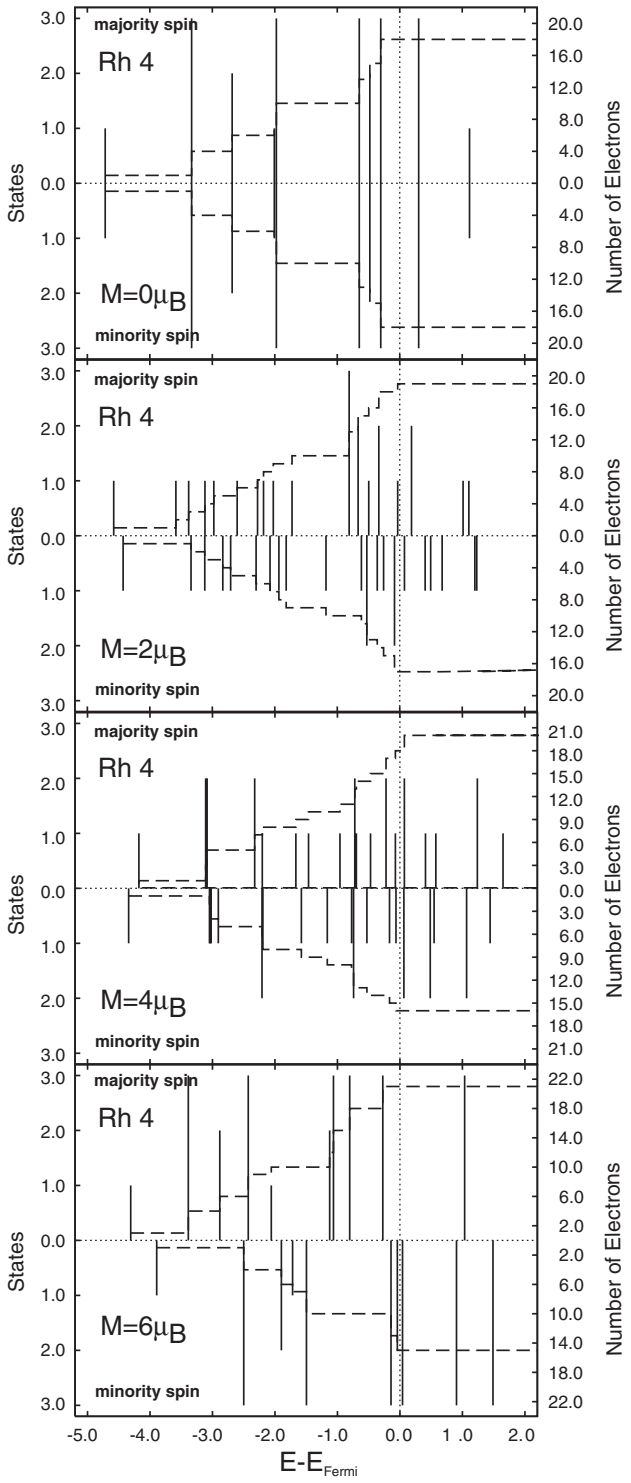

Figure 8. Electronic eigenvalue spectrum and integrated number of electrons per spin channel for tetrahedral Rh_4 clusters with $S = 0$ to 3 (top to bottom).

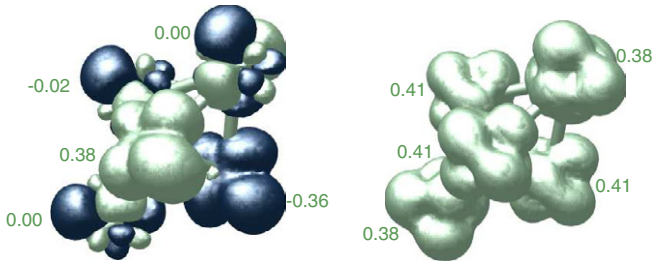

Figure 9. Local magnetic moments (in μ_B) and isosurface plots of the magnetization densities in trigonal bipyramids of Pd_5 for the $S = 0$ (left) and $S = 1$ (right) spin isomers. Note that for the $S = 0$ isomer the symmetry is reduced from D_{3h} to C_{2v}. The symbols are the same as in figure 5.

full T_d symmetry we observe a number of threefold- and twofold-degenerate eigenstates, the reduced symmetry of the $S = 1$ and 2 isomers lifts the degeneracy and leads to a much denser spectrum. For the highest-spin isomer, the state-dependent exchange splitting varies between 0.34 and 1.09 eV for the occupied eigenstates.

4.4. Pd_5 and Rh_5

For the pentamer Pd_5, we considered a square pyramid (D_{4h} symmetry) and an acute and a flat trigonal bipyramid (D_{3h}) (see figure 1). The most favourable structural isomer of Pd_5 is the trigonal bipyramid (TBP)—in agreement with the results of Moseler *et al* [23]—with a binding energy of 1.805 eV/atom and a total magnetic moment of 2 μ_B (0.41 μ_B/atom for the atoms making up the triangle and 0.38 μ_B/atom for the two atoms forming the caps). The length of the bonds forming the triangle is 2.65 Å, whereas the bonds with the caps are slightly shorter at 2.64 Å. Hence both the geometric and the magnetic structure differ only slightly from those of a double tetrahedron. The $S = 0$ isomer shows an antiferromagnetic distorted (C_{2v}) structure with two atoms in the central triangle carrying moments of about ± 0.37 μ_B, while the remaining three are almost non-magnetic. However, as shown by the magnetization densities (figure 9) this does not mean that there is no spin polarization at these sites. The C_{2v} point group has two mirror planes (parallel to the central triangle and passing through the three non-magnetic sites). The magnetization densities of the antiferromagnetically coupled sites have essentially $d_{x^2-y^2}$ character parallel to this last plane, while on the other three sites spin-up and spin-down electrons occupy orthogonal states extending perpendicular to this plane.

The most favourable spin isomer of the square pyramid structure has a binding energy of 1.798 eV/atom and a magnetic moment of 2 μ_B (0.43 μ_B/atom for the atoms making up the base, and 0.28 μ_B/atom for the atom forming the cap). The $S = 0$ isomer shows zero moment on all atomic sites. The structural energy difference between the stable magnetic isomers of the trigonal bipyramid and the square (both $S = 1$) is only 7 meV/atom, so both structures should be present in thermodynamic equilibrium. A flat trigonal bipyramid squeezed along the trigonal axis is a metastable configuration with a larger structural energy difference.

For the Rh_5 cluster we found the $S = 5/2$ ($M = 5$ μ_B) spin isomer of the square pyramid to be the ground state with $E_B = 3.028$ eV/atom. The atoms building the base have a bond length of 2.39 Å and a magnetic moment/atom of 0.97 μ_B; the capping atom is located at a distance of 2.58 Å from the atoms making up the base and has a magnetic moment/atom of 1.13 μ_B. Magnetic energy differences relative to the $S = 3/2$ and 7/2 isomers are very small, only 22 meV/atom and 11 meV/atom, respectively. For the trigonal bipyramid, the structural distortions relative to a double tetrahedron are much more pronounced than for Pd_5,

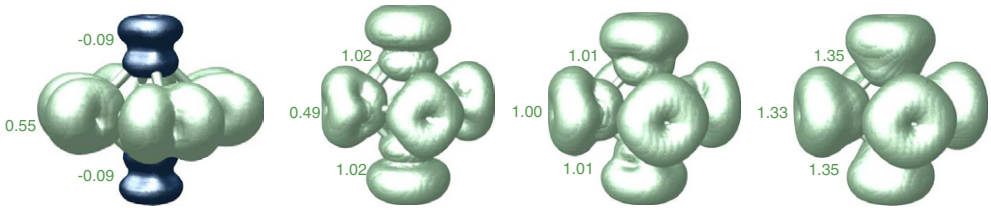

Figure 10. Isosurface plots of the magnetization densities of the $S = 1$–4 (from left to right) spin isomers of a (nearly) octahedral Rh_6 cluster. Dark surfaces surround regions of negative magnetization, light surfaces regions of positive magnetization. For the $S = 1$, 2, and 4 isomers the symmetry is lowered from O_h to D_{4h}. For the low-spin isomers, the local magnetic moments (in μ_B) are listed beside the atoms; for the $S = 3$ and 4 isomers the local magnetic moments are 1 μ_B and 1.33 μ_B, respectively, on all sites. See the text.

and we also calculate larger differences in the magnetic moments of the atoms at the basis and at the vertices. However, again in contrast to the Pd case, no antiferromagnetic components are found in any of the isomers of Rh_5. The stable magnetic isomer for both the acute and the flat trigonal bipyramids is $S = 7/2$. For the acute bipyramid the structural energy difference relative to the square pyramid is only 57 meV, and we note also only a very small magnetic energy difference between 12 and 23 meV for the low-spin isomers. Hence for the Rh_5 cluster a coexistence of different structural and magnetic isomers has to be expected. Our results for the ground state are in good agreement with those of Reddy *et al* [36], Chien *et al* [35] and Wang *et al* [73], but disagree with those of Aguilera-Granja *et al* [38] and Jinlong *et al* [13], who found the trigonal bipyramid with a magnetic moment of 1 μ_B respectively 3 μ_B to be the ground state of Rh_5.

4.5. Pd_6 and Rh_6

For the six-atom clusters the octahedron (symmetry O_h), the pentagonal pyramid (C_{5v} symmetry), and a pentagonal bipyramid with a vacant site in the central plane have been considered as possible structural isomers (see figure 1). For Pd_6 the $S = 1$ isomers are the magnetic ground state for all three configurations, but the magnetic energy differences for the $S = 0$ isomer are only of the order of ten meV/atom. For the Pd_6 octahedron, full O_h symmetry is conserved in both magnetic isomers, although the HOMO (minority spin) is threefold degenerate and only partially occupied (see figure 3). However, no Jahn–Teller distortion is produced. In the non-magnetic state, the non-degenerate HOMO of the majority electron is emptied, filling the HOMO of the minority spins.

For the pentagonal pyramid, the fivefold symmetry is reduced to C_{1h} (mirror plane through the axis of the pyramid) for both magnetic isomers; the $S = 0$ isomer is in fact weakly antiferromagnetic. The investigation of the non-magnetic spin isomer led to another metastable structure, a pentagonal bipyramid with a missing atom in the central plane (see figure 1). This structure has a higher symmetry (C_{2v} with two perpendicular mirror planes through the central axis and perpendicular to it) and a lower structural energy difference relative to the octahedron. Its $S = 0$ isomer (which is higher in energy by only 10 meV/atom) has an antiferromagnetic configuration with non-magnetic atoms in the central plane and moments of ± 0.36 μ_B at the vertices. Alternatively this structure may also be considered as consisting of three face sharing tetrahedra clustered along a central axis, or as a distorted octahedron. This interpretation is also suggested by the close similarity of the local magnetic moments, which all range within ± 0.01 μ_B around 0.33 μ_B. The structural energy difference of 42 meV is, however, not small

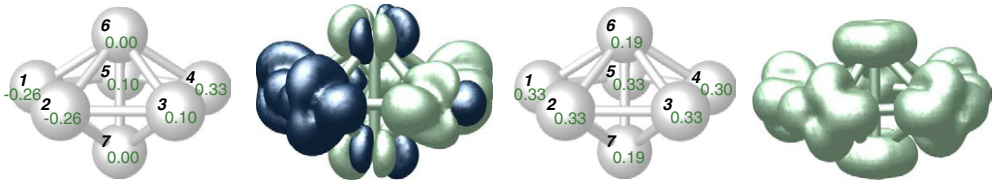

Figure 11. Local magnetic moments (in μ_B) and isosurface plots of the magnetization densities of the $S = 0$ (left) and $S = 1$ (right) spin isomers of a Pd_7 cluster forming a slightly distorted pentagonal bipyramid. Dark surfaces surround regions of negative magnetization, light surfaces regions of positive magnetization. See the text.

enough to suggest a coexistence of the two isomers in thermal equilibrium. Our results are in good agreement with those of Barreteau *et al* [27] and Moseler *et al* [23].

For the Rh_6 we found the octahedron with a magnetic moment of 6 μ_B to be the ground state. In addition to the magnetic ground state we identified four metastable spin isomers with $S = 0$–4; isosurfaces of their spin polarization densities are shown in figure 10. Only in the $S = 0$ state with non-magnetic atoms and in the $S = 3$ ground state with local atomic moments of exactly 1 μ_B on all atoms is the full octahedral symmetry conserved; for all other isomers it is lowered to D_{4h}. The magnetic configuration for $S = 1$ is ferrimagnetic, with small negative moments on the atoms located along the tetragonal axis. In contrast, the $S = 2$ state shows moments at the vertex sites which are twice as large as those of the atoms in the basal plane (for exact values of the local moments and interatomic distances, see again the supporting material). The structural distortions imposed by the constraint of assuming an intermediate spin state lead to larger magnetic energy differences for the $S = 2$ and 4 configurations than for the non-magnetic isomer (see table 2). For the pentagonal pyramid, the symmetry is reduced to C_{1h} for the low-spin isomers ($S = 1$ and 2), due to large differences in the magnetic moments of the atoms in the basis of the pyramid. For the $S = 3$ and 4 states, the cluster geometry is compatible with pentagonal (C_{5v}) symmetry, but the magnetic structure has lower symmetry (C_{1h} with a mirror plane through the axis and one of the basis atoms). Again we find an incomplete pentagonal bipyramid to be lower in energy than the pentagonal pyramid. In both cases, non-magnetic isomers are unstable; for the former the favoured magnetic isomer is $S = 2$, and no isomers with a lower magnetic moment are stable. The small structural energy difference is 36 meV. Studies of other researchers give conflicting results. Wang *et al* [37] and Chien *et al* [35] (DFT-GGA) and Barreteau *et al* [27] agree with our predictions, while Jinlong *et al* [13] and Reddy *et al* [36] (DFT-GGA) found the non-magnetic octahedron to be the ground state of Rd_6.

4.6. Pd_7 and Rh_7

For Pd_7 the cluster geometries explored in earlier studies [23, 24, 27] were a centred hexagon, a pentagonal bipyramid (PBP), an octahedron with a capped triangular face, and a polytetrahedral cluster. Because of this large number of structural isomers, we decided to search for the optimal geometry using a dynamical simulated annealing run. The DSA run converged both for Pd and Rh clusters—as expected from results of former researchers—to a distorted pentagonal bipyramid (PBP). For Pd_7, the spin isomer with a total magnetic moment of 2 μ_B (composed of magnetic moments of 0.33 μ_B (four atoms) and 0.30 μ_B (one atom) for the atoms forming the pentagon and 0.19 μ_B for the atoms located along the axis) with a binding energy of 1.985 eV/atom was found to be the ground state. The symmetry around the fivefold axis is broken; the relaxed cluster has C_{2v} symmetry. The same reduced symmetry is found for the $S = 0$ state with the antiferromagnetic configuration shown in figure 11. On the sites located

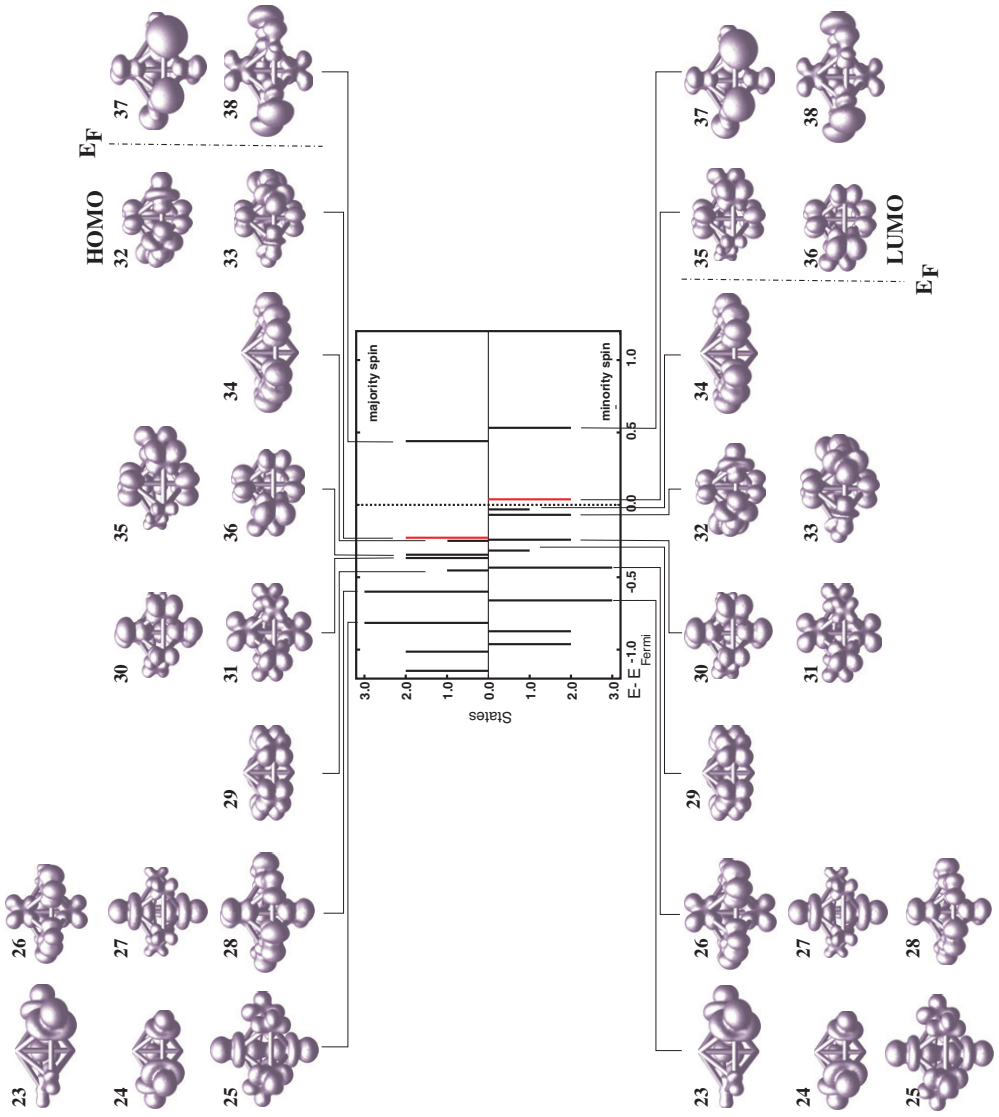

Figure 12. Spin-polarized electronic eigenvalue spectrum and isosurface plots of the electronic density distributions of eigenstates in the vicinity of the Fermi level, as calculated for the stable ($S = 1$) spin isomer of a Pd_7 cluster forming a slightly distorted pentagonal bipyramid. Eigenstates for minority electrons are numbered in order of increasing energy; eigenstates for minority electrons carry the number of their symmetry-equivalent counterparts. Note the re-ordering of eigenstates close to the Fermi level caused by the state dependence of the exchange splitting. See the text.

in the central plane, states with negative spin extend in the peripheral direction, whereas states extending perpendicular to the plane are occupied preferentially by spin-up electrons.

As an example of electronic eigenstates of the clusters, we present in figure 12 the spin-polarized electronic eigenvalue spectrum of the stable Pd_7 isomer (pentagonal bipyramid with $S = 1$), together with the electron density distributions of the states in the vicinity of the Fermi level. This analysis allows us to identify the exchange-split eigenstates with the same symmetry; all are compatible with an overall C_{2v} symmetry of the clusters.

Table 3. Energies of eigenstates for spin-up and spin-down states and exchange splitting (ΔE_{ex}) of the stable Pd_7 isomer (pentagonal bipyramid with ($S = 1$)); cf figure 12 and the text.

	Band No									
	19–20	21–22	23–25	26–28	29	30–31	32–33	34	35–36	37–38
Majority	−1.1464	−1.0138	−0.8152	−0.5994	−0.4530	−0.3636	−0.2268	−0.2426	−0.3466	0.4400
Minority	−0.962	−0.8731	−0.6600	−0.4335	−0.3155	−0.2410	−0.0905	−0.0383	0.0383	0.5322
ΔE_{ex}	0.1844	0.1407	0.1552	0.1659	0.1375	0.1226	0.1363	0.2043	0.3849	0.0922

The exchange splitting is found to be strongly state dependent. Within this interval the splitting varies between $\Delta E_{ex} \sim 0.10$ eV for the empty eigenstates 37 and 38 (for occupied eigenstates the smallest splitting of ∼0.12 eV is found for states 30 and 31) and $\Delta E_{ex} \sim 0.38$ eV for states 35 and 36, for details see table 3. The strong state dependence of the exchange splitting changes the energetic ordering of spin-up and spin-down states close to E_F. States 35 and 36 are occupied for majority and empty for minority electrons. Only these two degenerate states contribute to the spin density of the $S = 1$ isomer—a comparison of figures 11 and 12 demonstrates that the magnetization density is just the sum of the electron densities of these two degenerate states. This demonstrates that the magnetic structure is determined by states in the immediate vicinity of the Fermi energy.

A planar configuration in the form of a centred hexagon is metastable in $S = 0$ and 1 states, albeit with a relatively large structural energy difference of nearly 0.3 eV/atom. For both magnetic isomers the hexagonal symmetry is reduced to D_{2h}, with two atoms at opposite corners of the hexagon having a distance from the centre which is 0.45 Å ($S = 0$) and 0.17 Å ($S = 1$) larger than that for the other four atoms. Our results are in good agreement with those of Barreteau *et al* [27], Moseler *et al* [23], and Kumar *et al* [24].

For the Rh_7 cluster we found the pentagonal bipyramid (PBP) with a magnetic moment of 13 μ_B to be the ground state, but the energy of a 11 μ_B isomer is only 19 meV/atom higher. For all metastable magnetic isomers the pentagonal symmetry is reduced to C_{2v}, while the magnetic ground state conserves the fivefold symmetry C_{5h} around the axis of the bipyramid. Quite generally, the reduced symmetry is more apparent in the magnetic moments than in the cluster geometry. The strongest structural distortion is found for the $S = 11/2$ isomer, for which the interatomic distances along the periphery of the central plane differ by as much as 0.2 Å (for details see the supporting material); with decreasing magnetization the structural distortion is gradually reduced—for $S = 5/2$ (isomers with lower moments are unstable) the fivefold symmetry of the cluster geometry is nearly completely recovered (up to differences of 0.01 Å in the distances), but the magnetic symmetry is distinctly lower with moments of two times 0.72 μ_B, two times 0.78 μ_B, and 0.75 μ_B on the atoms forming the fivefold ring. The binding energy of the distorted centred hexagon (D_{2h} symmetry) with a magnetic moment of 13 μ_B amounts to 2.927 eV/atom; the structural energy difference is nearly 0.4 eV/atom (see table 2). Our results agree with those of other researchers concerning the equilibrium geometry, but disagree on the magnetic ground state. Reddy *et al* [36] and Barreteau *et al* [27] found the 9 μ_B PBP to be the ground state, whereas according to Aguileira-Granja *et al* [38], the non-magnetic PBP has the lowest energy.

4.7. Pd_8 and Rh_8

For the Pd_8 cluster we assumed an octahedral geometry with two adatoms capping triangular facets. Initially we considered a configuration in which the two capping atoms were placed in

front of opposite triangular faces on one side of the central square (see figure 1, configuration 8a); DSA produced a slightly different structure enabling the formation of a nearest neighbour bond between the capping atoms (see figure 1, configuration 8b*). As this configuration leads to a breaking of the bond between the two atoms forming the common edge of the capped triangles, the average coordination number remains the same, $N_C = 4.5$. However, in configuration 8a, the local coordination number varies between 3 and 6, whereas in configuration 8b, we have only four fourfold-and four fivefold-coordinated sites. For configuration 8a, the magnetic ground state has a magnetic moment of $4\mu_B$ (i.e. 0.52 μ_B for the atoms forming the base of the octahedron, 0.38 μ_B and 0.44 μ_B for the atoms at the vertices of the octahedron, and 0.55 μ_B for the capping atoms). For configuration 8b, a low-spin isomer with a magnetic moment of 2 μ_B (one half of atoms having a magnetic moment/atom of 0.28 μ_B and the other a magnetic moment/atom of 0.22 μ_B) was found to be the ground state. This configuration has the lowest total energy; the structural energy difference is 78 meV/atom compared to the most stable magnetic isomer with structure 8a. For all isomers, the point group symmetry is C_{2v}. Our result is in good agreement with that of Kumar *et al* [24] who found the distorted bicapped octahedron with a magnetic moment of 2 μ_B to be the energetically most preferred one.

For the Rh_8 cluster we compared both bicapped octahedron structures and spin isomers up to $S = 5$. The ground state is configuration 8b with a total magnetic moment of 10 μ_B (1.15 μ_B for the fourfold-coordinated sites and 1.35 μ_B for the fivefold-coordinated atoms). However, the magnetic energy difference compared to an isomer with $M = 8$ μ_B is only 4 meV/atom. Also the stable magnetic isomer of configuration 8a with $M = 8$ μ_B is only slightly higher in energy. We also calculate only minimal magnetic energy differences of a few millielectronvolts for the low-spin isomers (see table 1). Hence for the Rh_8 cluster many structural and magnetic isomers will coexist in thermodynamic equilibrium.

4.8. Pd_9 and Rh_9

For the Pd_9 cluster we assumed a capped pentagonal bipyramid (PBP) as the starting configuration for the static relaxations; DSA leads to a structure describable either as a trigonal antiprism with capped square faces or as an elongated trigonal prism with capped rectangular faces (see figure 1)—incidentally, this structure is one of the canonical coordination polyhedra discussed by Bernal as the building blocks of liquid and amorphous structures [74]. We also compared different spin isomers. For the capped PBP (which may be considered as a distorted polytetrahedral arrangement forming a fragment of an icosahedron) the symmetry is reduced to C_{1h} for all spin isomers; the (meta)stable spin isomer with a magnetic moment of 4 μ_B has a binding energy of 2.129 eV/atom. The magnetic energy differences compared to the low-spin isomers are only 11 and 21 meV for $S = 1$ and 0, respectively. The $S = 0$ isomer has an antiferromagnetic structure with small local moments.

The final structure after simulated annealing is a distorted double trigonal antiprism (see figure 1), consisting of three layers of nearly equilateral triangles, with the middle triangle rotated by 60°. Only for the high-spin isomer with $M = 4$ μ_B has the point group full trigonal D_{3h} symmetry, but the magnetic and structural ground state is the $S = 1$ isomer where the point group symmetry is reduced to C_{2v}. All symmetry is lost for the $S = 0$ isomer with an antiferromagnetic spin density distribution (see the supporting material for details). Again magnetic and structural energy differences are very small, only a few meV (see table 1), so all structural and magnetic isomers will be observed in thermal equilibrium.

For Rh_9 clusters we considered the same structures as were assumed for Pd_9. The stable spin isomers of the capped PBP and the double trigonal antiprism both have a magnetic moment of 11 μ_B; the structural energy difference is 25 meV/atom, and the magnetic energy differences relative to the states with moments of 9 and 13 μ_B are even smaller. The tendency to break the

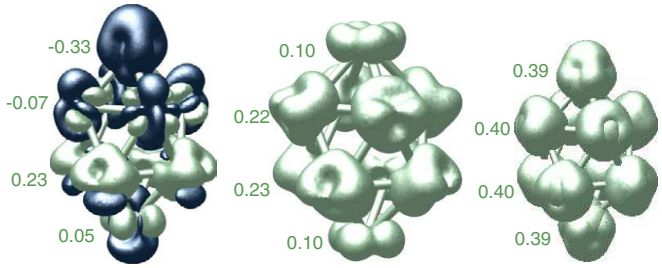

Figure 13. Local magnetic moments and isosurfaces of the magnetization densities for $M = 0$–4 μ_B for the Pd_{10} tetragonal antiprism with capped square faces (from left to right).

trigonal symmetry of the double antiprism is weaker than for Pd_9; both the magnetic ground state and the high-spin isomer have full D_{3h} symmetry, while the state with $M = 9$ μ_B is completely asymmetric (C_1). All spin isomers with the capped PBP have C_{2v} symmetry. For both Pd_9 and Rh_9 clusters the lowest-spin states of both structural isomers have ferrimagnetic and antiferromagnetic character, respectively. Aguilera-Granja *et al* [38] found a 14.58 μ_B spin isomer to be the ground state of Rh_9 (the origin of a non-integer value for the moment is unclear), whereas Reddy *et al* [36] (DFT-GGA) concluded that the 9 μ_B spin isomer is the most stable one. Both calculations consider only the capped PBP structure. Experimental studies [10] predict a magnetic moment/atom of 0.8 $\mu_B \pm 0.2$ μ_B.

4.9. Pd_{10} and Rh_{10}

For Pd_{10} clusters we compared three geometries, a tetragonal antiprism with capped square faces (C_{4v}—see configuration 10a in figure 1)—and a structure consisting of two edge sharing octahedra (10b) and a trigonal pyramid (10c) with atoms at the corners and the mid-edge positions. The 4 μ_B spin isomer of the edge sharing octahedra with $E_B = 2.185$ eV/atom was found to be the ground state; the global symmetry is D_{2h}. The two individual octahedra are only slightly distorted; their common edge is elongated by $\sim$0.1 Å. The magnetic energy differences relative to the $S = 1$ and 3 isomers are only 10 and 19 meV/atom, respectively. The magnetization of the $S = 2$ and 3 isomers is quite homogeneous, with local moments that are only slightly larger in the central plane. In contrast, the moments on these sites are strongly reduced in the $S = 1$ isomer.

The structural energy difference relative to the stable 4 μ_B spin isomer of the capped square antiprism is 45 meV/atom. The low-spin isomers of this configuration are only slightly higher in energy; their magnetization densities display an interesting antiferromagnetic structure in the $S = 0$ state (see figure 13), whereas in the stable $S = 2$ state all atoms have almost exactly the same moment of 0.40 μ_B. The $S = 0$ isomer is one of the cases where the atomic radii used for the calculation of the local DOS and magnetic moments could not be chosen such as to sum up to the correct total moment. The reason is that the complex magnetization densities centred at the individual moments are quite delocalized. Hence local moments are only semiquantitatively correct.

A third structural isomer is a tetrahedron with atoms at the vertices and slightly off the centre of all edges. The motivation for studying this structure is that all facets correspond to the closely packed (111) surfaces of the fcc crystal which have the lowest surface energy. The tetrahedral symmetry is broken in the low-spin isomer with $S = 1$ representing the magnetic ground state—in this case both the geometric and magnetic structure have C_{2v} symmetry. In the non-magnetic ($S = 0$) and in the high-spin isomers which differ in energy by only a

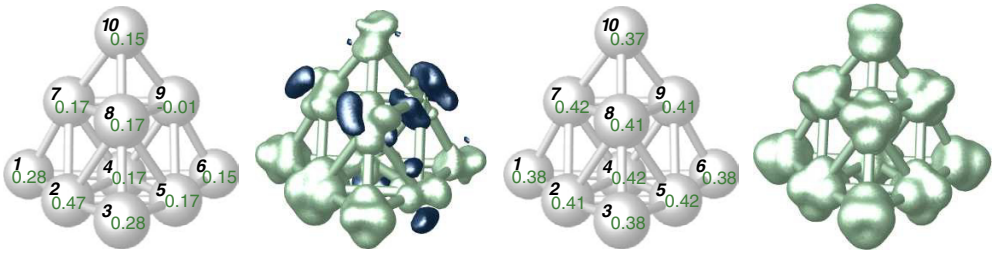

Figure 14. Local magnetic moments (in μ_B) and isosurfaces of the magnetization densities in tetrahedral Pd_{10} clusters with $S = 1$ (distorted C_{2v} symmetry) and $S = 2$ (T symmetry).

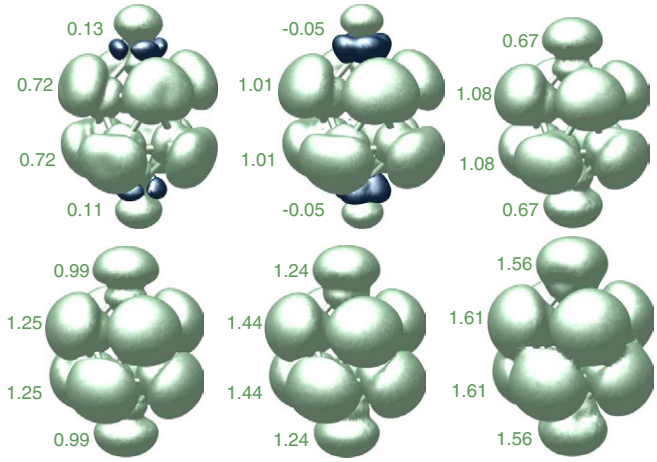

Figure 15. Local magnetic moments (in μ_B) and isosurfaces of the magnetization densities in Rh_{10} clusters with the structure of a capped tetragonal antiprism, for $S = 3$–8 (top left to bottom right). The stable magnetic isomer is $S = 8$. See the text.

few meV, the tetrahedral geometry (point group T) is completely recovered. Local magnetic moments and magnetization densities for $S = 1$ and 2 are shown in figure 14. This analysis shows that the equilibrium magnetic configuration is ferrimagnetic, with a substantial spin-down component on all low-moment sites. The structural energy difference relative to the bi-octahedral cluster is 69 meV.

For Rh_{10} the $S = 7$ spin isomer of the capped tetragonal antiprism with $E_B = 3.634$ eV/atom represents the ground state. For this structure all spin isomers between $S = 0$ and 6 are metastable; the spin density distribution (see figure 15) of the low-spin isomers shows an antiferromagnetic component at the apices which is, however, weaker than that found for the isostructural Pd_{10} cluster, compatible with C_{4v} symmetry. The $S = 0$ isomer is completely non-magnetic; the magnetization becomes more homogeneous with increasing spin. The stable magnetic isomer of the double octahedron is $S = 6$, with a structural energy difference of 27 meV/atom; for the large distorted tetrahedron a low-spin isomer with $S = 1$ represents the ground state, with a larger structural energy difference of 68 meV/atom. For the large Rh_{10} tetrahedron we observe a reduction of both the geometric and the magnetic symmetry to C_{1h} for all isomers (for details see the supporting material). Jinlong *et al* [13], using a spd tight binding model, found the 6 μ_B spin isomer of the twisted double square

pyramid to be the ground state. Experimental studies [10] predict a magnetic moment/atom of 0.8 $\mu_B \pm 0.2\ \mu_B$.

4.10. Pd_{11} and Rh_{11}

For Pd_{11} our starting configuration for the static relaxation calculations consisted of a pentagonal bipyramid with four capping atoms; the structural optimization led to a polytetrahedral cluster with C_{2v} symmetry. The stable magnetic isomer has a moment of 6 μ_B; the magnetization is distributed quite homogeneously over all atoms, varying only between 0.52 and 0.59 μ_B. The low-spin isomers are only slightly higher in energy; in the $S = 1$ state the magnetic symmetry is lower than the geometric symmetry (see the supporting material for details). DSA leads to a configuration consisting essentially of two distorted edge sharing octahedra with one additional atom. The position of this atom is such that a third, strongly distorted octahedron is formed. The optimized configuration has no apparent symmetry; the energetically most favourable spin isomer is $S = 3$, and it is lower in energy by 12 meV/atom than the polytetrahedral cluster. Magnetic energy differences from the low-spin configurations are only a few meV/atom.

The same configurations have also been explored for the Rh_{11} cluster, allowing for a larger range of magnetic moments. The ground state is the distorted polyoctahedral structure (point group C_1) with a magnetic moment of 13 μ_B and a binding energy of 3.674 eV/atom. For the polytetrahedral cluster the magnetic ground state has a lower moment of 5 μ_B only; all magnetic isomers have C_{2v} symmetry. The low-spin isomers are ferromagnetic. The structural energy difference is only 7 meV/atom; the magnetic energy differences are also very small for both structures (see table 2). Hence at finite temperatures, many structural and magnetic isomers will occur with comparable probabilities. Experimental results [10] indicate a magnetic moment/atom of 0.8 $\mu_B \pm 0.2\ \mu_B$, in reasonable agreement with the weighted average over the calculated magnetizations.

4.11. Pd_{12} and Rh_{12}

For the Pd_{12} cluster the starting configurations for the static relaxations were an icosahedron and a cubo-octahedron, both with a vacant centre. The final configuration after relaxation of the cubo-octahedral structure with a missing central atom consisted of a central cube with four capping atoms building four pyramids with a rectangular basis (see figure 1, configuration 12a). The magnetic ground state is $S = 2$ with full D_{4h} symmetry, which is also adopted by the magnetic isomers with higher spin. In a low-spin isomer with $S = 1$, the magnetic structure breaks the geometric symmetry; this ferrimagnetic configuration is completely asymmetric (see the supporting material for details). The icosahedral structure with a vacant centre is found to be unstable; it relaxes to a centred icosahedron with a vacant site in the outer shell (see figure 1, configuration 12b). The energetically most favourable magnetic isomer is $S = 3$, but with only minimal magnetic energy differences if the spin is reduced or enhanced by one unit. The fivefold rotational symmetry about an axis through the centre and the vacant site (point group C_{5v}) is realized only in the magnetic ground state; in the metastable magnetic isomers the symmetry is reduced to C_{1h}. This structure is lower in energy by 24 meV/atom than the capped cube. DSA leads to a structure which is best described as a polyoctahedral cluster: two edge sharing octahedra plus two more atoms added such that a further half-octahedron is formed; the optimized structure is plotted as figure 1, configuration 12c*, and the symmetry is only C_{1h}. The stable magnetic isomer is $S = 3$; this structure is still lower in energy by 17 meV than the incomplete icosahedron.

For Rh_{12} we compared the same structures as for Pd_{12}. The polyoctahedral cluster structure (configuration 12c* in figure 1; symmetry C_{1h}), which has been determined by dynamical simulated annealing, is found to have the lowest energy. The stable spin isomer of this structure has a magnetic moment of 16 μ_B (1.$\dot{3}$ μ_B/atom) and a binding energy of 3.714 eV/atom. The magnetic energy difference compared to an isomer with a moment of 15 μ_B is only of the order of a few meV/atom. The stable magnetic isomers of the incomplete icosahedron ($S = 9$) and of the capped cube ($S = 7$) are higher in energy by 33 meV/atom and 60 meV/atom, respectively. The symmetry of all isomers of the incomplete icosahedron is reduced to C_{1h}; states with $S \leqslant 4$ have a pronounced ferrimagnetic character. The capped cube has point group symmetry D_{4h} for the stable ($S = 7$) and the high-spin $S = 8$ isomers; the symmetry is reduced to C_{2h} for lower moment. Results from other researchers give conflicting results. Reddy *et al* [36] found the 8 μ_B spin isomer of the incomplete icosahedron to be the ground state of Pd_{12}, whereas Aguilera-Granja *et al* [38], using an spd tight binding model, found the 3 μ_B spin isomer to be the energetically most stable one. Experimental studies by Cox *et al* [10] provide a magnetic moment/atom of 0.59 $\mu_B \pm 0.12$ μ_B.

4.12. Pd_{13} and Rh_{13}

For the Pd_{13} cluster our starting structures for the static optimizations were the cubo-octahedron (O_h) and the icosahedron (I_h) (in contrast to the Pd_{12} cluster case, the central site is now occupied by a Pd atom). In addition, a third structure was generated by a dynamical simulated annealing run. Surprisingly, the cubo-octahedron was found to be unstable in this case also; the static relaxation led to a body-centred tetragonal structure with four capping atoms (see figure 1, configuration 13a). The stable spin isomer is $S = 2$; in this case (and for the higher-spin isomers) the symmetry is D_{4h}. The magnetic moment at the body-centred site is 0.69 μ_B; the atoms occupying the corners of the distorted cube have moments of 0.28 μ_B, while those of the capping atoms are only slightly lower with 0.26 μ_B. For the low-spin isomer with $S = 1$ both the molecular and the magnetic symmetry are reduced to C_{2h}; the magnetic structure has a weak antiferromagnetic component. The magnetic energy differences relative to the $S = 2$ state are 7 meV for $S = 1$ and 5 meV for $S = 3$.

Similar observations apply also to the icosahedron. The stable spin isomer is $S = 4$; for this high-spin solution the icosahedral I_h symmetry is conserved in the geometric and the magnetic symmetry. The symmetry is reduced to C_{2h} for the low-spin isomers ($S = 0$–2); their magnetization acquires a strong antiferromagnetic component (see figure 16). The $S = 0$ isomer is again one of the exceptional cases where the projection onto atomic spheres fail to produce accurate moments. The icosahedron is energetically favoured over the tetragonal structure derived from the cubo-octahedron, but DSA has identified an energetically more favourable structural isomer.

The structure resulting from the dynamical simulated annealing run is shown as figure 1, configuration 13c*. It may be considered as a cluster of three distorted edge sharing octahedra: two octahedra sharing one edge and a third one added in such a way that it shares edges with both and that one of its edges connects the vertices of the two octahedra. The average bond length is equal to 2.69 Å, individual bonds measure between 2.64 and 2.79 Å, and the point group symmetry is only C_{1h}. This structure has the shortest average bond length of all structural isomers, but a lower average coordination number than the icosahedron. The stable magnetic isomer is $S = 3$, but the magnetic energy differences from the low-spin isomers are exceedingly small ($\Delta E_{mag} \leqslant 3$ meV). The magnetization of this structure is surprisingly uniform; in the stable isomer the largest atomic moment is 0.51 μ_B, the smallest 0.45 μ_B. Figure 17 shows a graph of the relaxed cluster structure, featuring also the magnetic moments.

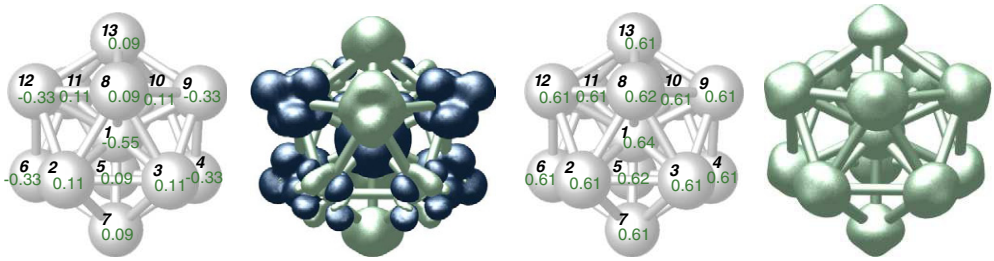

Figure 16. Geometric structure and local magnetic moments (in μ_B) and isosurface plots of the magnetization densities of the $S = 0$ and 4 spin isomers of a (nearly) icosahedral Pd_{13} cluster. Dark surfaces surround regions of negative magnetization, light surfaces regions of positive magnetization. See the text.

A side view of the cluster is particularly instructive as it demonstrates that it consists essentially of two close-packed sheets of atoms, in a close-packing stacking. This applies not only to the $N = 13$ cluster, but also to the stable structural isomers of the $N = 12$ and 11 clusters. This is a rather surprising result, suggesting that surface energies are a decisive structure-determining factor even for these very small clusters. The structural energy difference is 20 meV/atom compared to the icosahedron. Reddy *et al* [31] (DFT-GGA) found the icosahedron with a magnetic moment/atom of 0.43 μ_B for the central atom and 0.12 μ_B for the surface atoms to be the ground state of Pd_{13}.

For Rh_{13} we considered the same structures as for Pd_{13}. The spin isomer of the polyoctahedral cluster produced by DSA, with a magnetic moment of 15 μ_B, was found to represent the ground state ($E_B = 3.790$ eV/atom). The structural distortions of the individual octahedra are slightly larger than for Pd_{13}, with interatomic distances ranging between 2.53 and 2.79 Å. The icosahedron with a magnetic moment of 21 μ_B has a binding energy of 3.745 eV/atom. The capped body-centred structure (configuration 13a in figure 1) is most stable in a $S = 5/2$ state with D_{4h} symmetry, with a structural energy difference of 99 meV/atom relative to the ground state. Here it is interesting to observe that while in the Pd_{13} cluster with this structure the largest magnetic moment was found on the body-centred position, in the Rh_{13} cluster the magnetic moment is almost completely quenched (to 0.10 μ_B) at the central atom, while by far the largest moments are found on the capping atoms. The low-spin isomers of the icosahedron display again a strong antiferromagnetic component in the spin density distribution (see figure 18), which also triggers a substantial geometric distortion to C_{2h} symmetry, while in the high-spin isomers with $S = 15/2$ and $17/2$ the full I_h symmetry is conserved. These two isomers are higher in energy by only 3 and 6 meV respectively than the ground state with $S = 21/2$. Interestingly, at the highest magnetization, I_h symmetry is reduced to C_{2h} symmetry, with more pronounced distortions of the geometric than of the magnetic structure.

For the polyoctahedral configuration, the magnetization is quite homogeneous, with local magnetic moments between 1.03 and 1.27 μ_B for the stable isomer (see figure 19). The distribution of the local moments, with equal moments on a hexagon surrounding the central atoms, also suggests a slightly different view of this structure as a fragment of a face-centred cubic structure: a centred hexagon forms the fragment of a close-packed layer; atoms 2, 7, and 8 start the next layer of a close sphere packing; atoms 1, 5, and 13 are positioned so as to terminate dangling bonds at the fringe of the fragment. A side view of the structure demonstrates the layer structure of the optimized geometry.

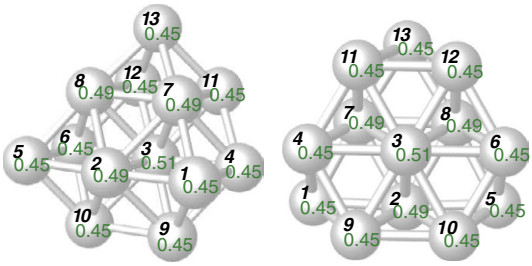

Figure 17. Structure of the stable Pd_{13} cluster ($S = 3$ isomer) with local magnetic moments (in μ_B, left), and a side view of the relaxed cluster (right). See the text.

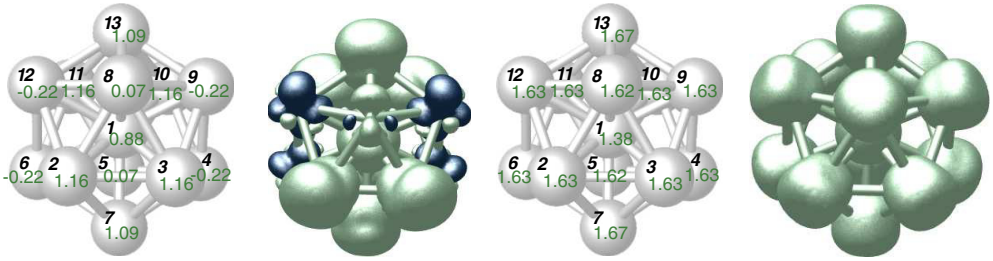

Figure 18. Geometric structure and local magnetic moments (in μ_B) and isosurface plots of the magnetization densities of the $S = 7/2$ and $21/2$ isomers of an icosahedral Rh_{13} cluster. Dark surfaces surround regions of negative magnetization, light surfaces regions of positive magnetization. See the text.

5. Summary and conclusions

In this work we have presented a comprehensive investigation of the structural, electronic, and magnetic properties of Pd_N and Rh_N clusters with up to $N = 13$ atoms. The novel aspects of our investigation are the following:

(i) The structural optimizations of the cluster by symmetry-unconstrained static total-energy minimization have been supplemented for larger clusters ($N \geqslant 7$) with a search for the ground state structure by means of dynamical simulated annealing. The dynamical structural optimization has led to the discovery of highly unexpected ground state configurations.

(ii) The spin-polarized calculations have been performed in a fixed-moment mode. This allows us to study coexisting magnetic isomers and leads to a deeper insight into the importance of magnetostructural effects.

For all clusters with nine or more atoms, the dynamical simulated annealing strategy has identified novel structures with a lower energy than any of the structural variants discussed so far in the literature: for $N = 9$ a double trigonal antiprism (similar to the canonical Bernal polyhedron for nine atoms); for $N = 11$ a structure of edge sharing octahedra, completed by one adatom; for $N = 12$ a similar configuration, but with two adatoms completing a half-octahedron; and for $N = 13$ a cluster of three octahedra. Alternatively, the last three configurations can also each be considered as a stacking of fragments of two close-packed planes, slightly distorted at the edges, i.e. as fragments of the bulk fcc structures of both elements. That even for such small clusters crystalline fragments should be preferred over non-crystallographic motifs achieving a higher average coordination (such as the icosahedron)

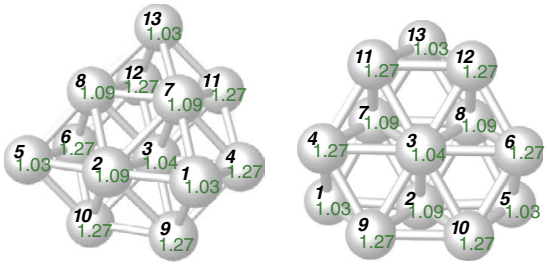

Figure 19. Structure of the stable polyoctahedral Rh_{13} cluster ($S = 15/2$ isomer) with local magnetic moments (left), and a side view of the relaxed cluster (right). See the text.

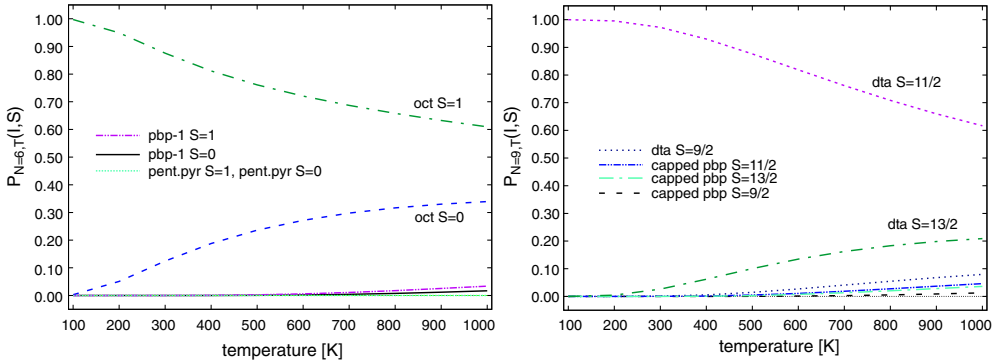

Figure 20. Left: probability $P_{N=6}$ (as a function of temperature) of a Pd_6 cluster adopting the structure of an octahedron (oct.), of a pentagonal pyramid (pent. pyr.), or of an incomplete pentagonal bipyramid (pbp) and spin states $S = 0$ or 1. Right: probability $P_{N=9}$ of a Rh_9 cluster adopting the structure of a double trigonal antiprism (dta) or of a capped pentagonal bipyramid (pbp) and spin states $S = 9/2$ to $13/2$.

is certainly quite surprising. It is also somewhat surprising that while an icosahedron represents at least a local minimum on the potential energy surface for the $N = 13$ clusters, a cubo-octahedron was found to be unstable and relaxed to a tetragonally distorted capped cube (which represents in turn only a local minimum).

With these new ground state configurations, the binding energy shows a very smooth variation with cluster size—it varies essentially proportionally to the square root of the average coordination number, emphasizing that in these transition metal systems, the size dependence is better understood in terms of even oversimplified tight binding arguments than in terms of shell model considerations relevant for jellium-like simple metal clusters. Our calculations demonstrate that structural energy differences can be small enough (a few tens of meV/atom) to lead to a finite probability for the formation of metastable cluster structures at higher temperatures.

A large effort has been spent, especially for Rh clusters, on investigating the coexistence of magnetic isomers. Quite generally, magnetic energy differences are much smaller than structural energy differences—for the larger clusters, the magnetic ground state is favoured over other magnetic isomers by only a few meV/atom. As a consequence, excited magnetic isomers exist even at ambient temperatures. As examples, we show in figure 20(a) the probability of finding an octahedral Pd_6 cluster in the $S = 1$ triplet and in the $S = 0$ singlet states—at $T \sim 500$ K, about 25% of the clusters lose their magnetic moments. In figure 20(b) a similar analysis for a Rh_9 cluster is presented. In this case, besides the $S = 11/2$ magnetic ground state

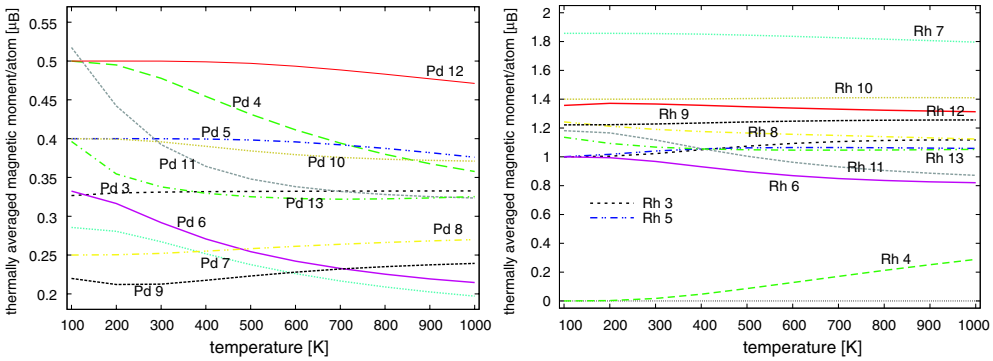

Figure 21. Thermally averaged magnetic moment/atom (μ_B) for Pd and Rh clusters as a function of temperature (K).

of the double trigonal antiprism, isomers with both higher ($S = 13/2$) and lower ($S = 9/2$) magnetic moments coexist at higher temperatures. In this case the diagram also shows that there is a finite probability of a coexisting structural isomer (the capped pentagonal bipyramid).

Figure 21 summarizes the results for the expected temperature dependence of the magnetic moments of Pd_N and Rh_N clusters. The average is over both magnetic and structural isomers. The surprising result is that the magnetic moment can increase as well as decrease with temperature, as in some cases low- and high-spin isomers are excited with almost the same probability. Examples of magnetic moments increasing with temperature are provided by the Rh_4 cluster (which is non-magnetic in the ground state) and the Rh_{12} cluster, with a lower magnetic energy difference for a high-spin isomer than for a low-spin isomer. For a Pd_9 cluster, the magnetic moment even shows a non-monotonic variation as a function of T—this is due to the fact that for the structural ground state configuration, magnetic isomers with higher and lower moment occur with comparable probability and that, in addition, at higher temperatures there is a finite probability of forming a high-spin structural isomer (cf the magnetic and structural energy differences listed in tables 1 and 2).

Our study also presents ample evidence for magnetostructural effects—the simple examples are the Pd_3 triangle, the Pd_4 tetrahedron, and the Pd_5 trigonal bipyramid; in all three cases, the symmetry of the cluster is lower in the non-magnetic $S = 0$ isomer than in the $S = 1$ ground state, and in all three cases, the $S = 0$ isomer is in fact not paramagnetic, but antiferromagnetic. Antiferromagnetic components of the magnetization densities and magnetically induced symmetry breaking have also been found in a number of other cases. Striking examples are the Rh_6 octahedron, where only the paramagnetic $S = 0$ and the stable $S = 3$ isomer adopt the full O_h symmetry while all other magnetic isomers are tetragonally distorted, and the icosahedral clusters: Pd_{13} has full icosahedral (I_h) symmetry only for the high-spin isomers, while for Rh_{13}, the icosahedral symmetry is reduced to orthorhombic both in the high- and low-spin limits. Altogether, the magnetism of Pd and Rh clusters shows a rich variety of phenomena which had hardly been explored up to now. The coexistence of ferromagnetic and antiferromagnetic components in the magnetization density might also be considered an indication of the possible existence of non-collinear magnetic structures. However, the appearance of antiferromagnetic components in the magnetization is always accompanied by a reduced symmetry of the cluster (see, e.g., figures 7 and 9). Hence, as previously demonstrated by Hobbs *et al* [61], frustration exchange interactions may perhaps be more efficiently released by distortions of the geometric structure than by a canting of the

magnetic moments. A definite answer on this would require the simultaneous optimization of all $6 \times N$ geometric and magnetic degrees of freedom of an N-atom cluster—which represents a formidable computational task beyond the scope of the present work.

The chemical properties of small clusters depend on their HOMO–LUMO gap and on the nature of the frontier orbitals. Our results compiled in tables 1 and 2 demonstrate a strong variation of the gap with the magnetization for a given structural isomer, and also between possible metastable structural variants. The analysis of the electronic spectrum (not reported in detail here) also points to changes in the nature of the frontier orbitals—the consequences for the chemical reactivity of the clusters remain to be explored.

Acknowledgments

This work was been supported by the Austrian Science Funds (Fond zur Förderung der wissenschaftlichen Forschung in Österreich—FWF) through the Science College 'Computational Materials Science'.

References

[1] Stara I, Nehasil V and Matolin V 1995 *Surf. Sci.* **331** 173
[2] Valden M, Aaltonen J, Kuusisto E, Pessa M and Barnes C J 1994 *Surf. Sci.* **307** 193
[3] Che M and Bennett M O 1989 *Adv. Catal.* **36** 55
[4] Zhu M J, Bylander D M and Kleinman L 1990 *Phys. Rev.* B **42** 2874
[5] Wu R and Freeman A J 1992 *Phys. Rev.* B **45** 7222
[6] Blügel S 1992 *Phys. Rev. Lett.* **68** 851
[7] Bellini V, Papanikolaou N, Zeller R and Dederichs P H 2001 *Phys. Rev.* B **64** 094403
[8] Spišák D and Hafner J 2003 *Phys. Rev.* B **67** 214416
[9] Bergara A, Neaton J B and Ashcroft N W 2003 *Int. J. Quantum Chem.* **91** 239
[10] Cox A J, Louderback J G and Bloomfield L A 1993 *Phys. Rev. Lett.* **71** 923
[11] Cox A J, Louderback J G, Apsel S E and Bloomfield L A 1994 *Phys. Rev.* B **49** 12295
[12] Ganteför G and Eberhardt W 1996 *Phys. Rev. Lett.* **76** 4975
[13] Jinlong Y, Toigo F and Kelin W 1994 *Phys. Rev.* B **50** 7915
[14] Douglass D C, Bucher J P and Bloomfield L A 1992 *Phys. Rev.* B **45** 6341
[15] Taniyamaand T, Ohta E and Sato T 1997 *Europhys. Lett.* **38** 195
[16] Balasubramanian K 1989 *J. Chem. Phys.* **91** 307
[17] Dai D and Balasubramanian K 1995 *J. Chem. Phys.* **103** 648
[18] Dai D and Balasubramanian K 1999 *Chem. Phys. Lett.* **310** 303
[19] Lee S, Bylander D M and Kleinman L 1989 *Phys. Rev.* B **39** 4916
[20] Valerio G and Toulhoat H 1996 *J. Phys. Chem.* **100** 10827
[21] Watari N and Onishi S 1998 *Phys. Rev.* B **58** 1665
[22] Lee K 1998 *Phys. Rev.* B **58** 2391
[23] Moseler M, Häkkinen H, Barnett R N and Landman U 2001 *Phys. Rev. Lett.* **86** 2545
[24] Kumar V and Kawazoe Y 2002 *Phys. Rev.* B **66** 144413
[25] Zhang W, Ge Q and Wang L 2003 *J. Chem. Phys.* **118** 5793
[26] Efremenko I and Sheintuch M 1998 *Surf. Sci.* **414** 148
[27] Barreteau C, Guirado-López R, Spanjaard D, Desjonquéres M S and Oleś A 2000 *Phys. Rev.* B **61** 7781
[28] Krüger S, Vent S, Nörtemann F, Staufer M and Rösch N 2001 *J. Chem. Phys.* **115** 22082
[29] Beznosjuk S A, Minaev B F, Dajanov R D and Muldakhmetov Z M 1990 *Int. J. Quantum Chem.* **38** 779
[30] Chen H, Krasowski M and Fitzgerald G 1993 *J. Chem. Phys.* **98** 8710
[31] Reddy B V, Khanna S N and Dunlap B I 1993 *Phys. Rev. Lett.* **70** 3323
[32] Goursot A, Papai I and Daul C A 1994 *Int. J. Quantum Chem.* **52** 799
[33] Harada M and Dexpert H 1996 *J. Phys. Chem.* **100** 565
[34] Nayak S K, Weber S E, Jena P, Wildberger K, Zeller R, Dederichs P H, Stepanyuk V S and Hergert W 1997 *Phys. Rev.* B **56** 8849
[35] Chien C H, Blaisten-Barojas E and Pederson M R 1998 *Phys. Rev.* A **58** 2196
[36] Reddy B V, Nayak S K, Khanna S N, Rao B K and Jena P 1999 *Phys. Rev.* B **59** 5214

[37] Wang L and Ge Q 2002 *Chem. Phys. Lett.* **366** 368
[38] Aguilera-Granja F, Rodríguez-López J L, Michaelian K, Berlanga-Ramírez E O and Vega A 2002 *Phys. Rev.* B **66** 224410
[39] http://cms.mpi.univie.ac.at/futschek
[40] Kresse G and Hafner J 1993 *Phys. Rev.* B **47** 558
[41] Kresse G and Hafner J 1994 *Phys. Rev.* B **49** 14251
[42] Kresse G and Furthmüller J 1996 *Phys. Rev.* B **54** 11169
[43] Kresse G and Furthmüller J 1996 *Comput. Mater. Sci.* **6** 15
[44] Wood D M and Zunger A 1985 *J. Phys. A: Math. Gen.* **18** 1343
[45] Perdew J P and Zunger A 1981 *Phys. Rev.* B **23** 5048
[46] Ceperley D M and Alder B J 1980 *Phys. Rev. Lett.* **45** 566
[47] Perdew J P and Wang Y 1992 *Phys. Rev.* B **45** 13244
[48] van Barth U and Hedin L 1972 *J. Phys. C: Solid State Phys.* **5** 1629
[49] Vosko S H, Wilk L and Nusair M 1980 *Can. J. Phys.* **58** 1200
[50] Blöchl P E 1994 *Phys. Rev.* B **50** 17953
[51] Kresse G and Joubert D 1999 *Phys. Rev.* B **59** 1758
[52] Jahn H A and Teller E 1937 *Proc. R. Soc.* A **161** 220
[53] Ullrich C A and Kohn W 2001 *Phys. Rev. Lett.* **87** 93001
[54] Aryasetiawan F and Gunnarsson O 1995 *Phys. Rev. Lett.* **74** 3221
[55] Svane A and Gunnarsson O 1990 *Phys. Rev. Lett.* **65** 1148
[56] Becke A D 1993 *J. Chem. Phys.* **98** 5648
[57] Lee C, Yang W and Parr R G 1988 *Phys. Rev.* B **37** 785
[58] Dederichs P H, Blügel S, Zeller R and Akai H 1984 *Phys. Rev. Lett.* **53** 2512
[59] Williams A R, Moruzzi V L, Kübler J and Schwarz K 1984 *Bull. Am. Phys. Soc.* **29** 278
[60] Schwarz K and Mohn P 1984 *J. Phys. F: Met. Phys.* **14** L129
[61] Hobbs D, Kresse G and Hafner J 2000 *Phys. Rev.* B **62** 11556
[62] Stillinger F H and Weber T A 1984 *J. Chem. Phys.* **80** 4434
[63] Jaswal S S and Hafner J 1988 *Phys. Rev.* B **38** 7311
[64] Knight W D, Clemenger K, de Heer W A, Saunders W A, Chou M Y and Cohen M L 1984 *Phys. Rev. Lett.* **52** 2141
[65] de Heer W A 1993 *Rev. Mod. Phys.* **65** 612
[66] Brack M 1993 *Rev. Mod. Phys.* **65** 677
[67] Heine V 1980 *Solid State Phys.* **35** 1
[68] Baletto F, Fortunelli A, Montalenti F and Mottet C 2002 *J. Chem. Phys.* **116** 3856
[69] Lin S S, Strauss B and Kant A J 1969 *J. Chem. Phys.* **51** 2282
[70] Lide D R (ed) 1995 *Handbook of Chemistry and Physics* 76th edn (Boca Raton, FL: CRC Press)
[71] Gingerich K and Cocke D 1972 *J. Chem. Soc. Chem. Commun.* **1** 536
[72] Schipper P R T, Gritsenko O V and Baerends E J 1999 *J. Chem. Phys.* **111** 4056
[73] Wang H, Haouari H, Craig R, Liu Y, Lombardi J and Lindsay D 1997 *J. Chem. Phys.* **106** 2101
[74] Bernal J D 1964 *Proc. R. Soc.* A **280** 299